Experimental and numerical investigations of plastic strain mechanisms of AISI 316L alloys with bimodal grain size distribution

Clément Keller, M. Calvat, B. Flipon, Fabrice Barbe

Version of Record: https://www.sciencedirect.com/science/article/pii/S0749641922000316
Manuscript_e0e0dad84468e3e32383bf3ea23b4125

Experimental and numerical investigations of plastic strain mechanisms of AISI 316L alloys with bimodal grain size distribution

C. Keller[a,b,*], M. Calvat[a], B. Flipon[c], F. Barbe[a]

[a]*Groupe de Physique des Matériaux, UMR CNRS 6634, Normandie Université, INSA Rouen, Univ. Rouen, 76000 Rouen, France*
[b]*Laboratoire Génie de Production, INP-ENIT, 65000 Tarbes, France*
[c]*Mines ParisTech, PSL - Research University, CEMEF, UMR CNRS 7635, 06904 Sophia Antipolis, France*

Abstract

In this article, the plastic strain mechanisms of AISI 316L with bimodal grain size distributions are investigated using experimental characterizations and numerical simulations. Using powder metallurgy routes, samples were first manufactured to obtain unimodal (both ultra-fine grained and coarse grained) and bimodal grain size distributions with different volume fractions of ultra-fine and coarse grain populations. These specimens were then studied mechanically by performing monotonic and loading-unloading tensile tests. Based on the numerical description of microstructures with similar characteristics than the experimental ones, full-field finite element analyses were also conducted using the Méric-Cailletaud crystal plasticity model modified to take into account a grain size strengthening. Using both experiments and simulations, deformation mechanisms were investigated. Results show that the grain size distribution greatly affects these mechanisms: both the long-range intergranular backstress and the distributions of stress and strain inside each grain population are modified. In particular, the formation of low stress channels and of localization shear bands expanding over tens of grains are observed. These modifications depend, however, on the volume fraction of each grain size population and on the spatial distribution of one with respect to the other. These results are then discussed in terms of grain population interactions, long range backstress and grain size contrast.

Keywords: Heterogeneous microstructure, bimodal grain size distribution, austenitic stainless steels, strain mechanisms, crystal plasticity, tensile behavior

1. Introduction

For the challenges of reductions of both operating costs and greenhouse gaz emissions, the industry, especially transportation, still need to enhance the strength of metallic materials. Theoretically, such improvements can be obtained mainly by two routes. The first one is based on the

*Corresponding author

microstructure modification in order to impede dislocation slip. Reduction in grain size, precipitation or cold work are different known mechanisms. The second one is linked to the material chemistry using alloying elements in a given matrix or more recently with equimolar high entropy alloys. In this latter case the objective is to increase the intrinsic resolved shear stress. Generally, these two routes are employed simultaneously to reach the desired mechanical properties.

Inside these different ways of mechanical properties improvements, the grain size reduction is the only one which may be effective for pure annealed metals without significant degradation in other material properties such as the electron conductivity, corrosion or irradiation resistance (Etienne et al., 2011; Hug et al., 2017; Lu, 2004; Radiguet et al., 2008). More than seven decades after the pioneering works of Hall and Petch (Hall, 1951; Petch, 1953), the grain size strengthening is still investigated (Dunstan and Bushby, 2014; Feaugas and Haddou, 2003, 2007; Meyers et al., 2006) with a particular focus on ultra-fine grained or nanocrystalline materials (Gleiter, 1989; Lu, 2004; Meyers et al., 2006; Pineau et al., 2016; Zhu and Langdon, 2005).

Decreasing the grain size in the submicrometric range, new deformation mechanims appear: dislocation storage progressively vanishes whereas grain boundary sliding takes place in the nanometric range (Meyers et al., 2006; Van Swygenhoven and Derlet, 2001), which may lead to superplasticity (Sergueeva et al., 2006). Thermally activated dislocation annihilation at grain boundaries has been also reported to be a dominant deformation mechanism for very low grain sizes (Bach et al., 2020; Isaev et al., 2016; Renk et al., 2019). For Ultra-Fine Grains (UFG) with average sizes of a few hundred nanometers, the small grain size significantly increases the yield stress as reported for many materials (Meyers et al., 2006). Unfortunately, the exceptional strength of nanocrystalline and UFG materials generally comes along with a substantial reduction in ductility and damage tolerance (Dao et al., 2007; Li et al., 2014; Meyers et al., 2006). This problem results from a limited work hardening capability, as dislocation storage and interactions are widely absent, favoring early strain localization. Dislocations are emitted from boundaries or interfaces, propagate through the grain and become absorbed at the boundaries (Van Swygenhoven et al., 2006). In addition, atomistic simulations suggest that dislocation absorption can easily induce damage at the numerous grain boundaries, causing early sample failure (Bitzek et al., 2009; Pan and Rupert, 2014). This ductility reduction represents a strong issue for the industrial use of such UFG metals due to their poor damage resistance or lack of forming ability.

To circumvent this detrimental decrease in ductility, different strategies have been discussed in literature. Addition of alloying element may induce nano precipitation or lead to amorphous grain boundaries which in turn may improve the material ductility (Cheng et al., 2007; Duchaussoy et al., 2021, 2019; Ludy and Rupert, 2016; Pineau et al., 2016; Rupert, 2016). Strain gradients present in heterogeneous microstructures have also been reported as beneficial for ductility. The concept of heterogeneous or gradient microstructures have gained interest in the recent years for the development of UFG/nanostructured materials (Li et al., 2018; Lin et al., 2020; Ma, 2006; Ma and Zhu, 2017; Sathiyamoorthi and Kim, 2020; Wu et al., 2015; Wu and Zhu, 2017). The heterogeneous microstructures indeed give rise to hetero-deformation induced hardening related to microstructural heterogeneities (Li et al., 2018; Ma and Zhu, 2017; Sathiyamoorthi and Kim,

2020; Wang et al., 2020, 2018; Wu and Zhu, 2017). This feature contributes to strength and strain hardening which counterbalances the lack of dislocation storage and hardenability observed for homogeneous UFG metals (Ma and Zhu, 2017).

For materials with ultra-fine grains, one possibility to introduce a heterogeneous character in the microstructure is based on the dispersion in grain sizes. Adding Coarse Grains (CG) inside a matrix of Ultra-Fine Grains (UFG) leads to bimodal or multimodal size distributions which have been proved to improve the ductility due to the larger strain hardening capacity of coarse grains (Dirras et al., 2010; Flipon et al., 2017, 2018a; Vajpai et al., 2016a,b; Zhang et al., 2015a, 2014). Modifying the volume fraction of UFG and CG may, hence, constitute a useful mean to optimize both yield stress and ductility.

In the literature, two manufacturing routes have been reported to generate bimodal grain size distributions: severe plastic deformation and powder metallurgy. These two strategies have been employed to investigate the influence of a bimodal grain size distribution on the mechanical behavior of pure metals (Dirras et al., 2010; Höppel et al., 2010; Orlov et al., 2013; Tingaud et al., 2015), titanium and aluminum alloys (Magee et al., 2012; Mompiou et al., 2018; Sharma et al., 2020; Vajpai et al., 2015) and also for steels (Dirras et al., 2010; Flipon et al., 2018a; Park et al., 2018; Zhang et al., 2017, 2015b, 2014; Zheng et al., 2017).

Experimentally, regardless the nature of the relationship between the spatial distribution of grains and their sizes (typically in the form of size gradients or a harmonic distribution or a random distribution), it has been reported that the volume fractions of the respective grain size populations is a prominent factor for controlling the flow stress (Dirras et al., 2010; Flipon et al., 2018a; Orlov et al., 2013; Zhang et al., 2014) or even, simultaneously, the flow stress and the fracture strain (Flipon et al., 2018a; Orlov et al., 2013). For harmonic structures, the origin of the larger material ductility has been found to relate to the Geometrically Necessary Dislocations (GND) generated at the interface between the UFG population and the CG population. Despite the large UFG volume fraction, these GND increase the strain hardening capability of the alloy which helps to sustain large strains (Li et al., 2020; Ma and Zhu, 2017; Zhang et al., 2014). These interactions between UFG and CG were also reported to increase the material backstress compared to a unimodal grain size distribution (Park et al., 2018; Wu et al., 2015; Wu and Zhu, 2017; Zhang et al., 2014; Zhu and Wu, 2019). For heterogeneous microstructures, opposite trend has been reported with a decrease in intergranular backstress due to the presence of CG inside the UFG matrix (Flipon et al., 2018a). This decrease in backstress reduces, in turn, the stress concentration in the vicinity of grain boundaries which could delay the embrittlement of the material and the further fracture. These opposite results reveal that in the context of a bimodal grain size distribution, a better knowledge of the interaction between each grain size population is needed to understand and predict the mechanical behavior of such alloys, in particular the role played by the spatial distribution of CG.

Numerically, different articles dealing with the investigation and prediction of the mechanical behavior of bimodal alloys have been published. In these articles, analyses were mostly performed using mean-field homogenization modeling (Berbenni et al., 2007; Joshi et al., 2006;

Kurzydłowski and Bucki, 1993; Zhu et al., 2006; Zhu and Lu, 2012) whereas full-field approaches of the grain size dependent polycrystalline plasticity were less employed (Flipon et al., 2020; Lin et al., 2020; Magee and Ladani, 2015; Wang et al., 2019). Using mean-field models, the influence of the grain populations volume fractions on the mechanical properties have been correctly reproduced (Berbenni et al., 2007; Joshi et al., 2006; Zhu et al., 2006; Zhu and Lu, 2012) allowing, in turn, the investigation of stress and strain distributions in such polycrystals. However, as reported by the authors in a previous article, the representation of each polycrystalline grain size population by a corresponding homogeneous equivalent medium (one medium per mean grain size), leads to a critical underestimation of the stress and strain heterogeneity, especially in the configuration of large grain size contrasts (Flipon et al., 2020). Although possibilities exist to account for locally induced grain boundary interactions in mean-field modeling (Taupin et al., 2010, 2013), such an approach does not enable to address questions on the local scale grain-to-grain interactions according to the spatial distribution of the grains and their respective sizes. Full-field modeling with a high resolution on the description of the bimodal microstructure and on the related intragranular strain mechanisms provides a mean to better understand the effect of the bimodal grain size distribution on the stress and strain distribution.

Following these literature results, several questions arise: (i) what are the mechanisms responsible for the improvement in ductility in bimodal materials? (ii) what is the role played by the grain size contrast and spatial coarse grains distribution? (iii) What relevant information could be drawn from full-field polycrystalline plasticity to describe and explain the characteristic strain mechanisms governing the constitutive behavior of bimodal materials?

The objective of this study is to provide answers to these questions by the investigation of the mechanical behavior of AISI 316L steel with bimodal grain size distributions on the basis of a framework including coupled experimental and numerical aspects. On the one hand, the tensile behavior of such alloys manufactured by powder metallurgy has been investigated as a function of the volume fraction of UFG and CG and of their corresponding sizes. On the second hand, based on the microstructural characterization of the samples, representative microstructures have been generated using Voronoi-Laguerre tessellations. These numerical microstructures have then been employed to investigate in details, by means of crystal plasticity finite element analyses, the stress and strain distributions inside polycrystals with bimodal distributions. Both experimental and numerical studies lead to valuable results about the understanding of the mechanical behavior of such polycrystals.

The article is organized as follows. The two first sections are dedicated to the presentation of the experimental and numerical procedures, respectively. Experimental and numerical results are presented in the third section and discussed in the fourth one. This discussion is focused on the plastic behavior of each grain populations, the intergranular backstress and the effect of grain size ratio.

2. Experimental and material procedure

2.1. Sample elaboration

The investigated samples were obtained using powder metallurgy routes. The general purpose was to manufacture samples with large grain size distributions with different size contrasts between the smallest and largest grains and different volume fractions of each grain population. To this aim, three different AISI 316L powders were prepared: (i) a commercial powder of gaz atomized single-crystal particles of 3 µm, used as is to constitute a population of Fine Grains (FG); (ii) a commercial powder of gaz atomized polycrystalline particles of 45 µm with an average grain (crystal) size of 15 µm, used as is to constitute a population of Coarse Grains (CG); (iii) the 3 µm single-crystal powder particles which were ball-milled to obtain a nanostructured powder with scattering domains of around 15 nm and which led to 0.4 µm grains after sintering, themselves constituting a population of Ultra-Fine Grains (UFG). This ball-milling step was performed during 2h using ethanol as process control agent. The rotation speed was set to 500 rpm (more details about the powder milling can been found in previous articles (Keller et al., 2016; Marnier et al., 2014)). Figure 1 provides Scanning Electron Microscopy (SEM) images of the three powders. Despite the 316L grade, α phase is largely dominant over the γ one in these powders due to the non-equilibrium powder atomization process and, also, to the ball-milling (Keller et al., 2016; Marnier et al., 2014).

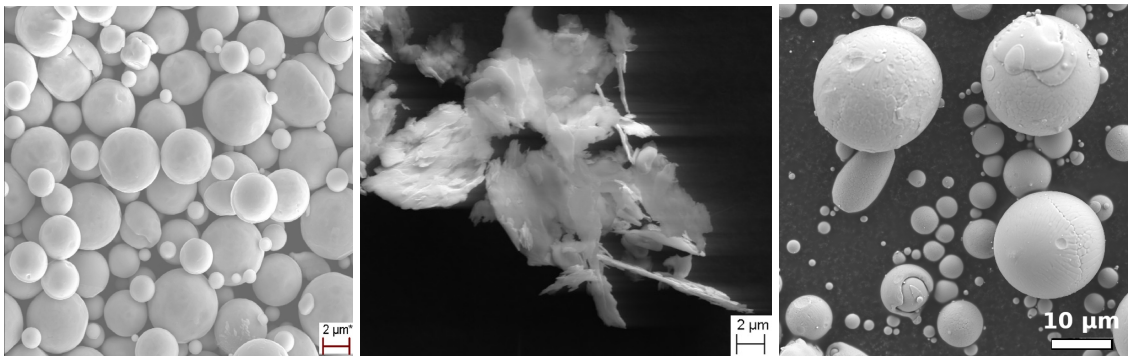

(a) (b) (c)

Figure 1: Scanning electron microscope observations of the precursor powders used for the sample manufacturing: (a) as-received powder with single-crystal 3 µm particles, (b) powder as obtained after the ball-milling of the single-crystal 3 µm particles and (c) as-received polycrystalline-powder particles with a mean size of 45 µm.

To obtain the bimodal microstructure, the CG, FG and UFG powders were combined with different volume fractions in order to investigate the role played by this parameter on the mechanical behavior. Powder ratios of 75/25, 50/50 and 25/75% were employed. Three sample series were obtained mixing UFG and FG powders (series 1), UFG and CG powders (series 2) and FG and CG powders (series 3). Based on these powder mixtures, cylinders of 50 mm diameter and 8 mm height were sintered using Spark Plasma Sintering (SPS; FCT System GmbH HD25, 50 MPa, 1150 °C, 300s, see (Keller et al., 2016; Marnier et al., 2014) for more details). In order to compare

the mechanical behavior of samples with bimodal grain size distributions to unimodal ones, samples using 100% UFG, FG and CG were also sintered using different conditions in order to obtain average grain sizes ranging between 0.4 (100% UFG powder) and 15 μm (100% CG powder). This unimodal series is labelled series 0 in the following paragraphs.

Dog bone shaped specimens with 9.5x6x1 (Lxlxw) mm gauge length were cut by electron discharge machining from these cylinders. These tensile test specimens are represented on Figure 2. Table 1 summarizes the characteristics of the different sintered samples: series number, grain size of each population, corresponding volume fraction, the size ratio between each population and the density analysed using the Archimede method. This density ranges from 95 and 98.7 % depending on the precursor powder characteristics due to both residual pores and oxide formation (Flipon et al., 2018a; Keller et al., 2016).

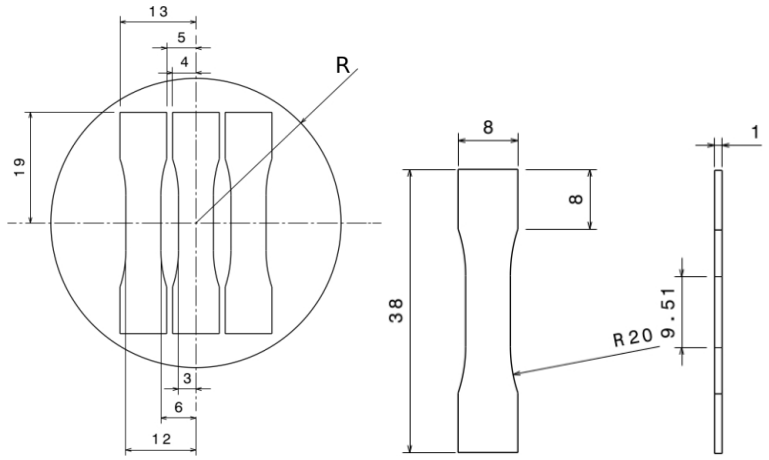

(a) (b)

Figure 2: (a) Overview of the positions of the tensile test specimens on the SPS cylinder prior to machining and (b) their geometry. Dimensions are expressed in mm. The SPS cylinder radius is R=50 mm.

Table 1: Microstructural characteristics of unimodal and bimodal samples manufactured by powder metallurgy and spark plasma sintering. UFG: Ultra-Fine Grain - FG: Fine Grain - CG: Coarse Grain. The last two columns are dedicated to the yield stress and fracture strain of each sample series. They are discussed in section 4.

Serie	Uni- or Bimodal	Size (µm)			Size ratio	Vol. fraction (%)		Relative	Yield stress	Fracture
		UFG	FG	CG	CG/(U)FG	(U)FG	CG	density (%)	(MPa)	strain
0	Unimodal	0.3	/	/	/	100	0	95.4	741	0.02
0	Unimodal	0.7	/	/	/	100	0	94.7	654	0.06
0	Unimodal	0.95	/	/	/	100	0	95.1	637	0.067
0	Unimodal	/	1.0	/	/	100	0	96.0	589	0.07
0	Unimodal	/	1.4	/	/	100	0	96.0	421	0.13
0	Unimodal	/	3	/	/	100	0	98.0	350	0.4
0	Unimodal	/	/	15	/	0	100	98.2	251	0.45
1	Bimodal	0.3	3	/	10	25	75	98.4	327	0.43
1	Bimodal	0.3	3	/	10	50	50	97.5	334	0.4
1	Bimodal	0.3	3	/	10	75	25	96.8	366	0.37
2	Bimodal	0.3	/	15	50	25	75	97.6	377	0.24
2	Bimodal	0.3	/	15	50	50	50	97.6	425	0.2
2	Bimodal	0.3	/	15	50	75	25	95.2	663	0.08
3	Bimodal	/	3	15	5	25	75	97.3	321	0.41
3	Bimodal	/	3	15	5	50	50	98.7	345	0.42
3	Bimodal	/	3	15	5	75	25	98.2	363	0.39

2.2. Microstructural and mechanical characterization

In order to characterize in details the initial microstructure of each sample series, SEM observations using secondary electrons and Electron Back-Scattered Diffraction (EBSD) were performed on a 30 kV field emission gun JEOL 7900 after conventional metallurgical sample preparation (mechanical grinding followed by a final step of electropolishing). Transmission Electron Microscopy (TEM) observations were also carried out to observe the initial dislocation structures (JEOL 2010 FX operating at 200 kV). To this aim, thin disks were extracted from the sintered rough material and electropolished for observations using a twin-jet electropolishing device.

For the mechanical testing, specimens were subjected to strain rate controlled tensile tests on a servohydraulic 25kN MTS machine. Using a conventional 8 mm gauge length extensometer, a strain rate of 2.10^{-4} s^{-1} was applied in order to reduce the viscoplasticity contribution on the mechanical behavior. Two kinds of tensile tests were performed, monotonic and loading-relaxation-unloading. As documented in previous articles (Dickson et al., 1984; Feaugas and Haddou, 2003; Keller et al., 2011), these former tests enable to characterize the isotropic and kinematic hardening linked respectively to the effective stress and the long-range backstress (Feaugas and Haddou, 2003). These two stress components are related to different interactions of mobile dislocations with the microstructure. The effective stress, represented by the loading surface radius, is linked to bulk dislocation storage and short range interactions due to forest dislocations or small coherent precipitates. The backstress, estimated using the center of the loading surface, is related to long range interactions between mobile dislocations and strong defects like heterogeneous dislocation structures, incoherent precipitates or grain boundaries. The knowledge of the evolution of these stress components with strain gives valuable information on the plasticity mechanisms. More details on the computation of these two stress components and their physical significances can be found elsewhere (Feaugas and Haddou, 2003; Keller et al., 2011).

3. Numerical procedure

The aim of the numerical investigation is to provide complementary analysis with respect to the experiments and to analyze the specific mechanisms involved in bimodal polycrystals. Crystal Plasticity Finite Element (CPFE) simulations of tensile tests were performed to investigate the stress and strain fields, the activated slip systems or the effect of the CG spatial distribution. For the sake of simplicity and computation time, these analyses were restricted to a given grain size ratio between CG and UFG.

3.1. Single crystal constitutitve behavior

Full-field modeling of size dependent polycrystal plasticity with a high resolution of the microstructure generally needs a compromise between the representativity of the microstructure (in terms of number of grains), the quality of the mesh refinement and computation costs. In this context, where internal lengths play a prominent role, non-local physics-based constitutive models such as strain gradient crystal plasticity (Arsenlis and Parks, 2002; Cordero et al., 2010; Evers

et al., 2004a,b; Fleck et al., 1994; Keller et al., 2012; Marano et al., 2021; Shu and Fleck, 1999), Cosserat or micromorphic approaches (Chang et al., 2016; Forest, 2008; Forest et al., 2000; Ling et al., 2018) barely allow acceptable computation times. For this study, a pragmatic approach consisting in the introduction of a size dependent term in the single crystal constitutive model was adopted. Among the different available crystal plasticity formulations, the Méric-Cailletaud model was chosen to conduct the numerical analyses (Méric and Cailletaud, 1991; Méric et al., 1991). This model, extensively used in CPFE analyses and for a large variety of mechanical problems (Barbe et al., 2001a,b; Barbe and Quey, 2011; Barbe et al., 2009; Benedetti and Barbe, 2013; Bouchedjra et al., 2020; Diard et al., 2005; Farooq et al., 2020; Flipon et al., 2020; Gérard et al., 2013; Guerchais et al., 2014; Guery et al., 2016; Guilhem et al., 2018; Yang et al., 2019; Zouaghi et al., 2016), makes a transposition of the macroscopic well-known Chaboche hardening law (Chaboche, 1989) to the glide system scale. With the introduction of the grain size dependence on the resolved shear stress, this modified model has been proved to correctly reproduce, at the microscopic and macroscopic level, the grain size strengthening (Flipon et al., 2020). The following paragraphs briefly describe the different constitutive laws of this model.

The material viscoplastic behavior is described by equation 1 which links the plastic shear rate ($\dot{\gamma}^s$) of the slip system s to the resolved shear stress τ^s and isotropic (r^s) and kinematic (x^s) hardening terms through an additive formulation. Plastic flow occurs on the system s when the resolved shear stress τ^s reaches a critical value τ_c^s.

$$\dot{\gamma}^s = \left\langle \frac{|\tau^s - x^s| - r^s}{K} \right\rangle^n \operatorname{sign}(\tau^s - x^s) \tag{1}$$

K and n describe the Norton viscosity.

In the original formulation, isotropic hardening is described by equation 2 with p the cumulated plastic strain. r_0 corresponds to the onset of plasticity whereas Q and b describe the saturating state of this non-linear hardening. h^{su} is an interaction matrix between slip systems. This matrix is described by 6 independent terms corresponding to the Self-Hardening (SH), Glissile-Junction (GJ), Lomer-Cottrel (LC), Hirth-Lock (HL), Cross-Slip (CS) and Coplanar (CP) dislocation interactions. According to this law, the resolved shear stress on system s increases in a non-linear way and takes into account the hardening due to the interaction with other slip systems (u).

$$r^s = r_0 + Q \sum_{u=1}^{12} h^{su} \left(1 - e^{-bp^u}\right) \tag{2}$$
$$\text{with } \dot{p}^u = |\dot{\gamma}^u|$$

For the sake of simplicity, as only monotonic tensile tests are considered in this study, no kinematic hardening was taken into account ($x^s = 0$).

In order to account for the grain size dependence of the flow stress, a Hall-Petch term is introduced in the definition of the resolved shear stress r^s. This solution is commonly adopted in many studies dealing with large scale polycrystalline plasticity (Berbenni et al., 2007; Lavergne et al., 2013; Lu et al., 2019; Phan et al., 2015). It indeed advantageously enables to include the prominent effect of the grain size on the macroscopic properties from a minimal number of parameters.

As defined in equation 3, this Hall-Petch term depends on the hardening coefficient k_g and on the internal length d_g. As reported previously by the authors (Calvat et al., 2021), this internal length can be defined either by the size of the considered grain - and is thereby uniform over the grain -, or by the distance to the grain boundary of the considered local point. This second proposal is meant to account for the increase in the density of geometrically necessary dislocations due to the interactions with the grain boundaries. With this internal length, the resolved shear stress depends on the position of the considered point with respect to the closest grain boundary. Analyses conducted from the macroscale to the intragranular scale of unimodal and bimodal polycrystals have shown that the effect of the choice of this internal length is significant only on the very local intragranular scale. In the present study, the retained internal length is the grain size.

$$r_g^s = r_{0\,g} + Q \sum_{u=1}^{12} h^{su} \left(1 - e^{-bp^u}\right) + \frac{k_g}{\sqrt{d_g}} \tag{3}$$

$r_{0\,g}$ is the critical resolved shear stress for an infinite grain size.

The model parameters, already identified for 316L in a previous study (Flipon, 2018; Flipon et al., 2020), are summarized in table 2.

Table 2: Crystal plasticity parameters identified for the considered SPS manufactured 316L steel (Flipon et al., 2020).

E (GPa)	ν	Q (MPa)	b	K (MPa.s$^{\frac{1}{n}}$)	n	h_{SH}	h_{CP}	h_{HL}	h_{CS}	h_{GJ}	h_{LC}	$R_{0\,g}$ (MPa)	k_g (MPa.µm$^{-1/2}$)
200	0.3	10	9.06	9	24	1.00	4.40	4.75	4.75	4.75	5.00	34.3	200

All simulations were performed with the Z-set software (Z-set, 2021) in the small deformation framework. Consequently, no strain level larger than 0.05 was considered for the tensile test simulations, and all stresses and strains values are expressed using the engineering definition.

3.2. Numerical microstructure description

The numerical analyses of bimodal grain size distribution effects on polycrystals plasticity are based on microstructures generated by generalized Voronoi tessellations. This approach, as compared to studies where an actual - experimentally characterized - 2D or 3D polycrystal is represented within a FFT or FE mesh (Lin et al., 2020; Proudhon et al., 2016), enables to conduct the analyses from a predetermined set of characteristic metrics (a minima the mean grain size of each grain population). Hence, it is possible to explore the effects of these metrics over a fully

controlled range.

Inside the generalized Voronoi framework, the Laguerre tessellations algorithm is used. As explained in literature (Quey and Renversade, 2018), it consists in subdividing space not only from the positions of Voronoi cells nuclei but also by a weight assigned to each nucleus. The weight acts as a radius defining the zone of influence of a nucleus and thereby provides a mean to control the sizes of polyhedra. As compared to a classical Voronoi tessellation, a Laguerre tessellation enables to reproduce given grain size and sphericity distributions (Quey and Renversade, 2018). It also provides an efficient way to reproduce a large variety of complex microstructures as illustrated in (Flipon et al., 2018b), especially for bimodal polycrystals.

In the present study, the objective is to focus on model microstructures where only the mean grain size of each grain population (UFG, FG and CG) and their respective volume fractions are taken into account for the comparisons with experiments. The microstructure is generated with the Neper software and then meshed with tetrahedral elements from the procedure of tessellation regularization enabling to obtain high quality unstructured meshes with grain boundaries strictly conforming to finite element boundaries (Neper, 2021; Quey et al., 2011). A detailed description of the procedure for bimodal polycrystal generation can be found in (Flipon et al., 2020).

Figure 3 summarizes the process in the 2D model case of a single CG embedded in a "matrix" of FG. In Figure 3(a), each dot represents a cell nucleus and the size of the dot corresponds to its weight. A zone of exclusion has been previously set around the central CG nucleus. Figure 3(b) and 3(c) show respectively the results of the Laguerre tessellation and of the free meshing into tetrahedra. The color code represents the crystallographic orientations of the grains with respect to the vertical (tensile) direction. In the present case, these orientations correspond to a random distribution.

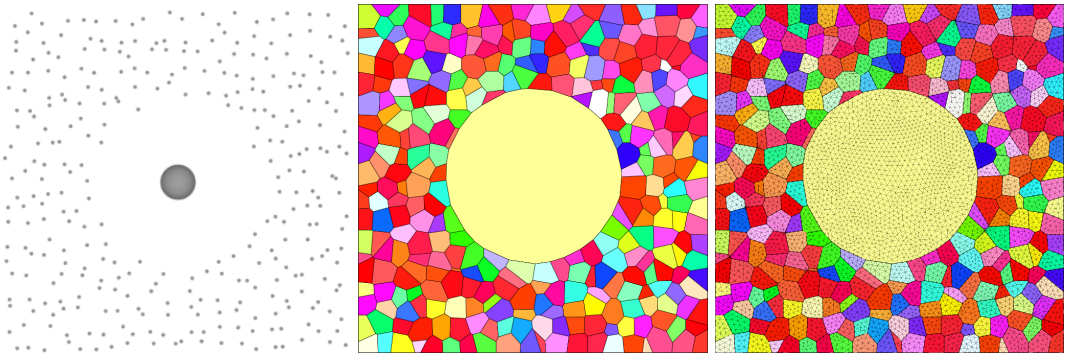

(a) (b) (c)

Figure 3: Main steps of the generation of a numerical polycrystal with a single coarse grain embedded in a matrix of fine grains: (a) positions and weights of the cell nuclei, (b) Laguerre tessellation and (c) free meshing of the tessellation.

As reported in (Flipon et al., 2020), a 2D-extruded bimodal polycrystal must contain at least 9 CG to be considered as a Representative Volume Element from the viewpoint of the macroscopic properties. Bimodal aggregates were hence generated using the procedure described above using a fixed number of 9 CG. A ratio of 10 between the sizes of CG and UFG has been considered, with UFG and CG having respective mean grain sizes of 0.5 and 5 μm, respectively. These grain sizes for both grain populations approximately correspond to the series 1 of experimental samples. Besides, this ratio sets up favorable conditions of a robust and efficient processing for the meshing and the resolution of the mechanical problem (fewer meshing iterations, larger time-step increments).

As presented on Figure 4, vertical displacements were exerted onto the top and bottom faces of the polycrystal to reproduce the tensile test. Multiple Point Constraints were set on the lateral faces such as to enforce them to remain parallel to their initial position and to account for the mean effect of the material surrounding the considered polycrystalline slice. This solution of a 2D-extruded microstucture and of the set boundary conditions has been shown to provide a macroscopic response which is in good agreement with that of a three-dimensional representative volume element of the polycrystalline medium (Flipon et al., 2020).

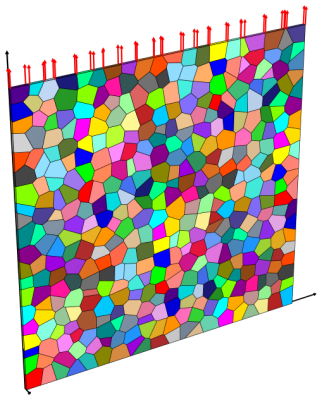

Figure 4: Presentation of the boundary conditions for finite element simulations

To investigate the role played by the spatial distribution of the CG, two kinds of bimodal aggregates were generated, featuring 9 CG inside a matrix of UFG. In the first case, referred to as "BM-iCG", the CG are *isolated* (or diluted) within the matrix in the sense of homogenization theories: to a first *a priori* approximation, a single CG could be considered to interact only with the UFG matrix. The second case corresponds to the general case where a CG can be either isolated or in contact with another CG such as to constitute a *cluster*, and is referred to as "BM-clCG". These aggregates were generated with the following constraints on the spatial distributions of nuclei:

- A minima, there should be 4 FG between the boundary of a CG and the outer boundary of the aggregate; this choice is meant to minimize the effect of boundary conditions on the CG constitutive response;

- for the isolated configuration (BM-iCG), two CG must be separated by at least 3 FG;
- for the clustered case (BM-clCG), there is no constraint on CG relative positions.

It is worth noting that, the mean grain size of each grain population being prescribed, the volume fraction of CG depends on these constraints but also on the user-set total number of grains inside the aggregate. Among the different aggregate generation runs, the two polycrystals presented in Figures 5(a,b) were considered for analysis. The isolated configuration contains 3645 FG and the volume fraction of CG is about 17%. In the clustered configuration, 1632 FG are present and CG volume fraction is about 30%. The use of a smaller number of grains was necessary in order to limit the distance between CG clusters, which would, in turn, favor interactions between clusters and promote strain localization.

The difference in CG volume fraction is known to affect the macroscopic properties with, to a first degree approximation, a linear dependence to this volume fraction (Flipon et al., 2020). It was further shown that the deviation of the macroscale stress response from the linear mixture rule approximate was increasing with the volume fraction of CG, which could be a consequence of the reduction of the distance between CG or ultimately their clusterisation. In the present study, the attention is more focused on the effect of FG-CG interactions on the local stress and strain fields than on the macroscopic properties and in this context of study the difference in CG volume fraction between the isolated and the clustered cases is expected not to impair the analyses.

In order to establish reference data to which bimodal polycrystals plasticity could be compared, and consecutively to examine the effects of the bimodality, microstructure with unimodal grain size distributions were also generated. They are referred to as “UM-UFG” and “UM-CG” for the respective mean grain sizes of 0.5 and 5 μm. They have the same microstructure, presented on Figure 5(c), containing 400 grains.

For each microstructure, random grain orientations were assigned to all the grains. These orientations cover the entire standard triangle for face centered cubic materials as described in Figures 5(d,e,f) for BM-iCG, BM-clCG and the unimodal aggregates respectively. Each grain is colored according to its crystallographic orientation.

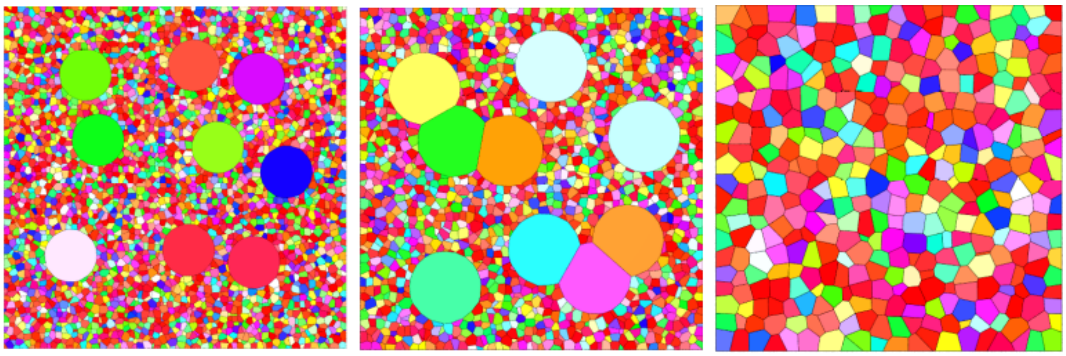

(a) BM-iCG (b) BM-clCG (c) unimodal case

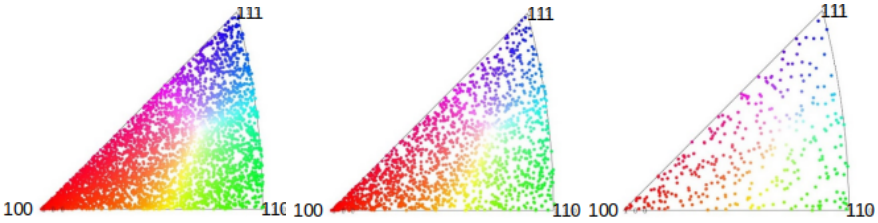

(d) BM-iCG (e) BM-clCG (f) unimodal

Figure 5: (a), (b) and (c) 2D-extruded numerical polycrystals under consideration in this study, respectively in the case of *isolated* coarse grains (BM-iCG), clustered coarse grains (BM-clCG) and the unimodal distribution (UM-UFG and UM-CG). (d), (e) et (f): associated grain orientations with respect to the vertical tensile direction, in the standard triangle. The colors of the grains in the tessellations correspond to their crystallographic orientations.

4. Experimental results

4.1. Initial microstructure characterization

The grain orientation maps of three bimodal samples are shown on Figure 6(a,b,c). They were elaborated from the powder series 1, 2 and 3 respectively, each with a volume fraction of grain populations UFG/CG equal to 75/25.

For series 1 and series 2 samples, a heterogeneous spatial distribution of the grain population is observed (Figure 6(a) and (b), respectively). Moreover, as expected, a large grain size contrast is observed for those samples. For series 3 specimens illustrated in Figure 6(c), this particular size contrast is no longer visible. This figure does not reveal any preferential grain orientation which is confirmed by the maximal pole densities of the pole figure (not represented here) that are lower than three M.R.D. (Multiple Random Distribution) ensuring isotropic mechanical behavior. For each analyzed sample, the UFG and CG average grain size is reported in table 1. Second phases (non indexed areas) are also encountered in the grain boundaries due to the powder and sample oxidation during the elaboration process. As analysed in details in a previous article, the oxide volume fraction is about 8% (Keller et al., 2016).

A view, provided by TEM, on the initial dislocation structures is given in Figure 6(d) for a sample of series 2 which exhibit the largest grain size contrast. As observed on other TEM images, the

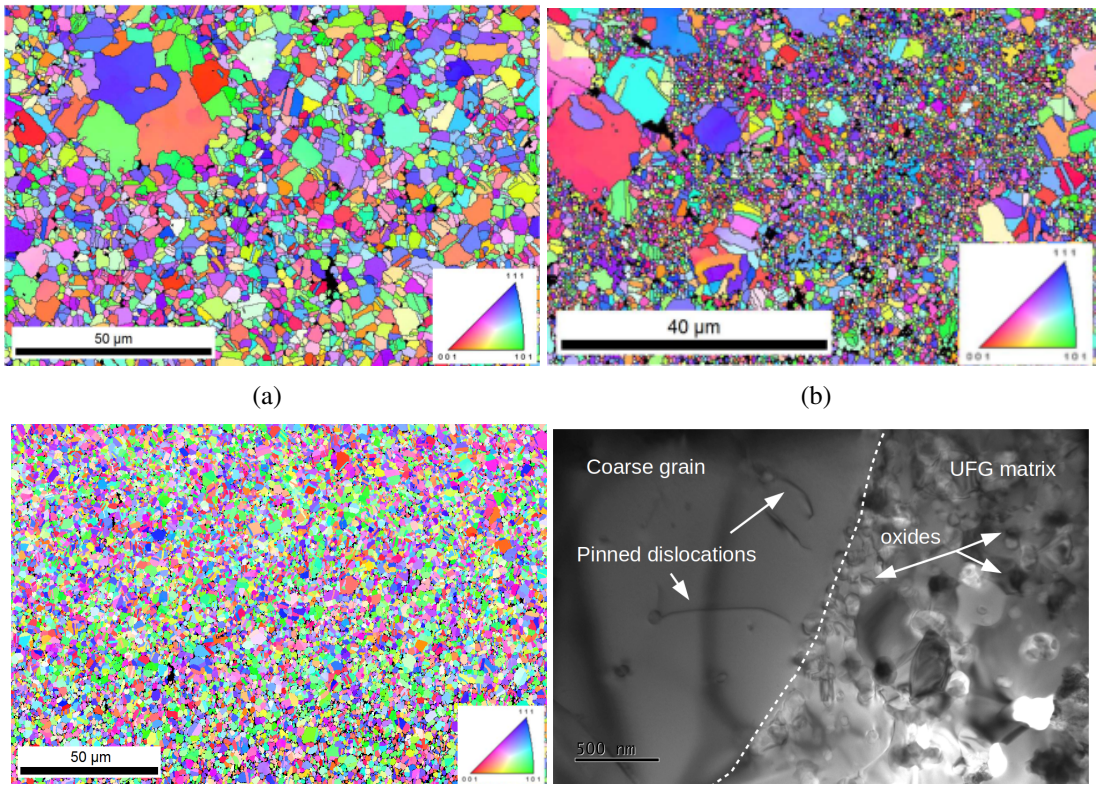

(a) (b)

(c) (d)

Figure 6: (a), (b), (c) Grain orientation maps of bimodal samples featuring the following grain populations (resp.): UFG/FG (series 1), UFG/CG (series 2), FG/CG (series 3) and (d) TEM observation of the initial dislocation structure for a UFG/CG sample.

initial dislocation density is slightly larger for CG than for UFG. This is in accordance with the propensity of plastic slip to occur more within CG than within UFG during the powder compaction and further sintering. Dislocation segments and tangles are observed, especially for CG without heterogeneous dislocation structures. Despite the difference between CG and UFG populations, the initial dislocation density remains low for all samples revealing the fully recrystallized character of the material. Moreover, it ensures that any difference in the mechanical behavior of a sample with respect to another will only be due to the differences in grain size distribution.

4.2. Mechanical characterization

Firstly, in order to investigate the mechanical behavior of the different sample series, monotonic tensile tests were performed up to fracture. Stress-strain curves are shown on Figure 7(a,b,c,d) for the respective sample series 0 (unimodal) and series 1, 2 and 3 (bimodal). For each figure dealing with a bimodal sample, the two extreme cases where there is 100% of one or the other grain size population is also represented. They simply correspond to the stress-strain curves of the unimodal samples with the matching grain size.

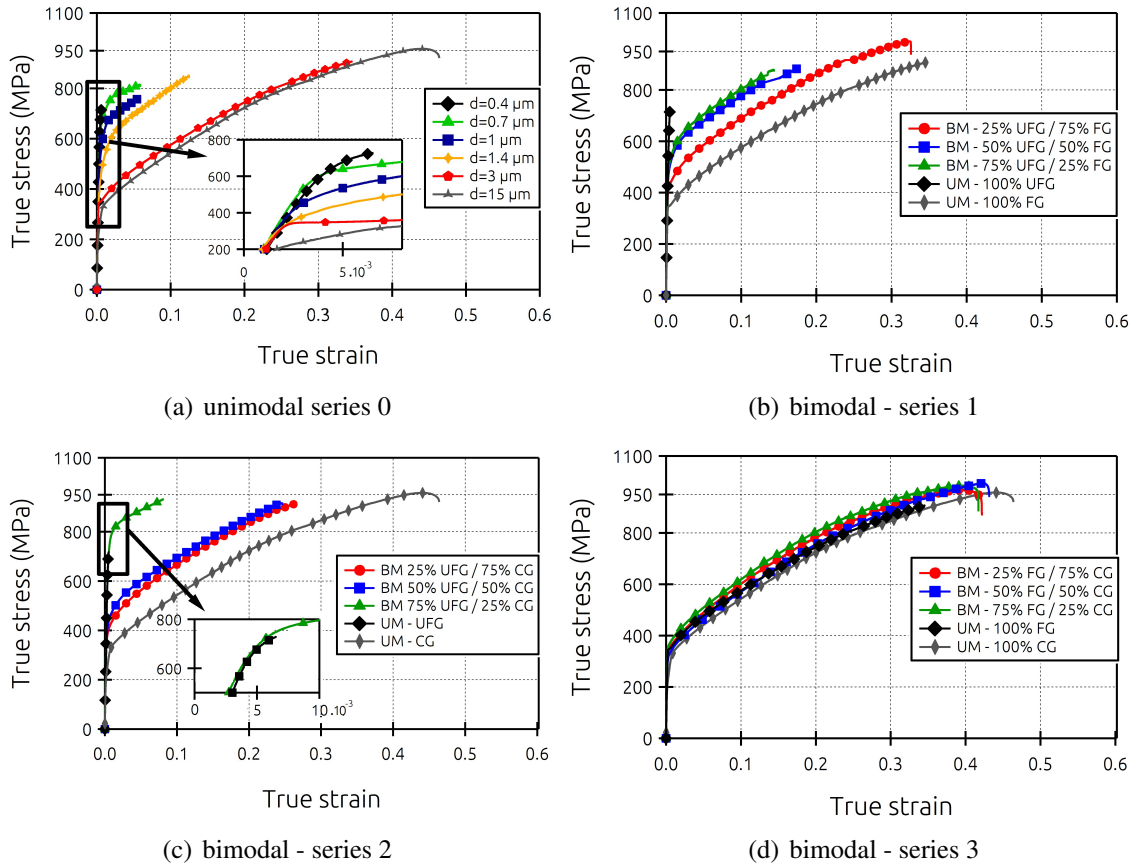

(a) unimodal series 0

(b) bimodal - series 1

(c) bimodal - series 2

(d) bimodal - series 3

Figure 7: Tensile curves of the different specimens characterized experimentally in this study: (a) unimodal samples - series 0; (b) bimodal samples - series 1; (c) bimodal samples - series 2 and (d) bimodal samples - series 3.

For the unimodal samples, the grain size strengthening associated to a decrease in grain size from 15 to 0.4 μm induces an increase in yield stress from 300 MPa to 750 MPa. However, as expected, this rise in yield stress decreases the plastic strain to failure, which itself is almost null for the lowest grain size (see the inset of Figure 7(a)).

For the bimodal series, both the grain size contrast and the volume fractions of the grain size populations influence the mechanical behavior. Independently of the grain size ratio, the larger the volume fraction of ultra-fine grains, the larger the yield stress and the lower the plastic strain to failure. For series 1, using an UFG matrix and a grain size ratio of 10, the stress level difference between the tensile curves related to the lowest and highest volume fractions of UFG/CG is about 100 MPa. The difference is much larger, about 300 MPa, in the case of series 2 with a grain size contrast of 50 and a matrix of UFG. In this case, the sample with the largest volume fraction (75%) of UFG exhibits a yield stress close to the one of the unimodal UFG (see the inset of Figure 7(c)), with a plastic strain to failure at 0.08. For this sample series, a decrease from 75 to 50% in the volume fraction of UFG strongly decreases the yield stress from 730 to 420 MPa. In the case of series 3 with a FG matrix and a grain size ratio of 5, the stress levels of the three bimodal tensile curves are similar.

Table 1 summarizes the mean stress and mean fracture strain associated to each sample series characterized mechanically in tension. Comparisons of both state variables between samples with unimodal and bimodal grain size distribution clearly highlight the positive influence of the bimodal configuration on ductility when both a UFG matrix and a large grain size ratio are employed. In that case, as compared to unimodal samples, ductility is increased with a reduced loss in yield stress.

Secondly, loading/relaxation/unloading tensile tests were carried out for the unimodal and bimodal samples of series 2, which exhibit the largest effect of the grain size distribution. Figure 8(a) provides an exemple of the complete tensile curve (series 0) for this kind of test. Figure 8(b) presents a magnified view on a loading/relaxation/unloading sequence and describes the decomposition of stress into three different components: thermal effective, athermal effective and backstress.

For the unimodal samples (series 0), the plots in Figures 8(c) and 8(d) represent the evolution of the backstress and effective stress as a function of the axial strain, respectively. Due to its dependence on the grain size (Feaugas and Haddou, 2003; Keller et al., 2011), the backstress displays a strengthening by a factor 3 between the lowest and the largest grain size. For the effective stress, the grain size strenghtening is reduced as this stress component depends only slightly on the grain size (Feaugas and Haddou, 2003). The average magnitude of the effective stress is in good agreement with values reported in literature for the same alloy with a conventional grain size (Feaugas and Haddou, 2003).

Concerning the bimodal samples of series 2, the changes in backstress and effective stress as a function of strain are presented in Figure 8(e,f) respectively. For each flow stress component, three

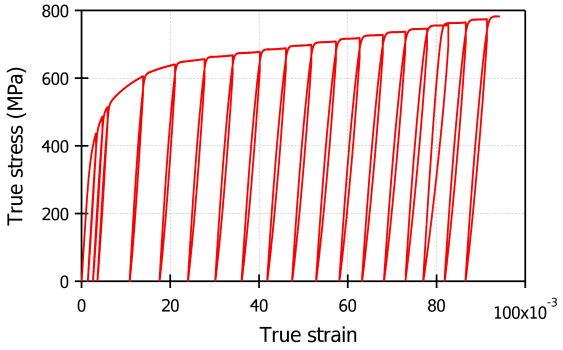

(a) illustration of a loading/relaxation/unloading tensile curve

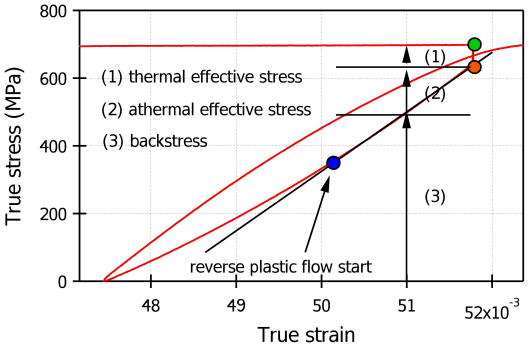

(b) example of loading/unloading loop

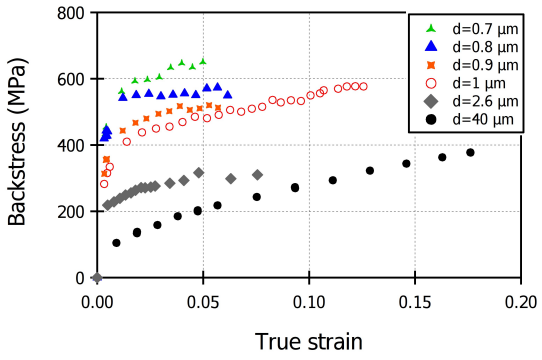

(c) unimodal series 0

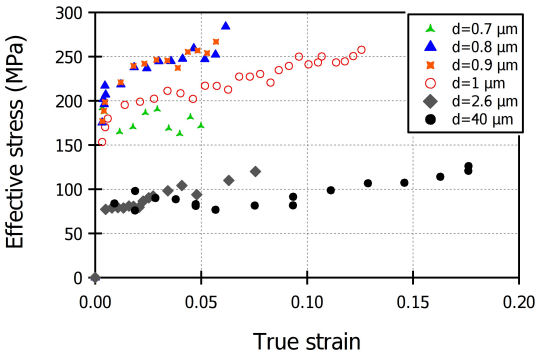

(d) unimodal series 0

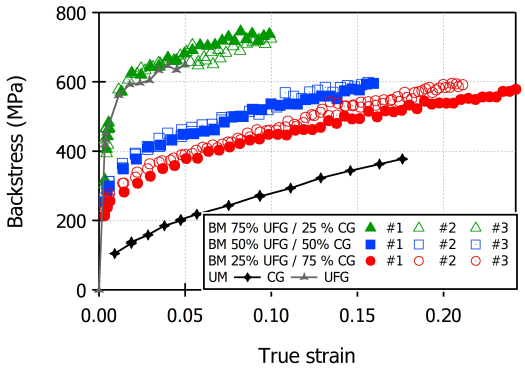

(e) bimodal series 2

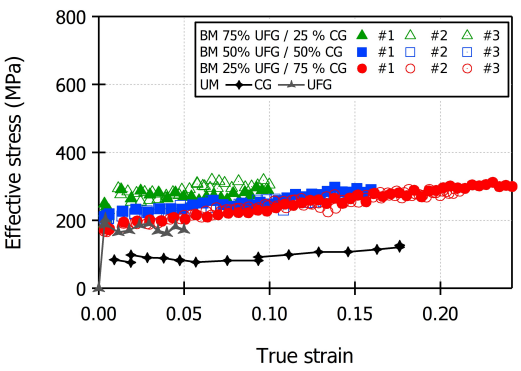

(f) bimodal series 2

Figure 8: Evolution of the flow stress as a function of strain during experimental tensile tests: (a) illustration of a general loading-relaxation-unloading test, (b) exemple of a loading-relaxation-unloading sequence for the computation of the flow stress components, (c) backstress, unimodal samples; (d) effective stress, unimodal samples; (e) backstress, bimodal samples - series 2 and (f) effective stress, bimodal samples - series 2.

volume fractions of UFG/CG are considered, and for each volume fraction, three different samples have been used, which enables to check the reproducibility of the results. As the effect of the grain size distribution is lower for the series 1 and 3, no stress partition analysis were performed for them. The observed values of the backstress depend clearly on the volume fraction of UFG: as for the flow stress, the larger the UFG volume fraction, the higher the backstress. It can be noted that the backstress value of the 75% UFG / 25%CG is similar to the one of the 0.7 μm-grain-size unimodal sample (no backstress could be measured from the 0.4 μm-grain-size UM sample since its fracture occurs in the transition between elasticity and plasticity). For the effective stress, the volume fraction of UFG only slightly affects this flow stress component: it is of the same order than in the unimodal specimens. It is worth noting that Park et al. (2018) have reported an increase of the backstress from a unimodal to a harmonic bimodal grain size distribution. In the present case of random bimodal samples, a reduction of the backstress is observed, and the effective stress remains almost constant. This highlights the peculiarity of the relationship between the spatial nature of the bimodal grain size distribution and the backstress, which is the subject of further discussion in Section 6.2.

5. Crystalline plasticity modeling

The experimental results clearly revealed that a bimodal grain size distribution affects the mechanical behavior with an increase in plastic strain at failure without strong modification of the yield stress if a small volume fraction of CG is introduced within the UFG matrix. In that case, the yield stress and ductility are controlled by the grain size contrast between the two grain populations. The backstress is then the main affected component of the flow stress. In order to better understand the role played by the coarse grains inside the UFG matrix, following the procedure described in section 3, crystalline plasticity modeling was considered. The following paragraphs describe, first, for comparison purpose, the constitutive behavior of the unimodal polycrystals. To this aim, macroscopic tensile curves, stress and strain fields alongside with an analysis of the activated slip systems are proposed. Then, a similar analysis is performed for the two bimodal polycrystals in the isolated and clustered configurations to highlight the influence of the grain size distribution.

5.1. Unimodal polycrystal responses

The macroscopic tensile curves of the two unimodal polycrystals with different mean grain sizes, i.e. 0.5 μm UFG and 5 μm CG, are given in Figure 9. As defined in the constitutive laws (see eq. 3), the model is able to correctly reproduce the grain size strengthening associated with the decrease in grain size between the two samples. The comparisons with the experimental tensile curves for UFG (d=0.7 μm) and CG (d=15 μm) reveal a good agreement between simulations and experiments. As the strain hardening does not depend on grain size in the model formulation, the strain hardening rate is similar for the two samples when plasticity is fully established.

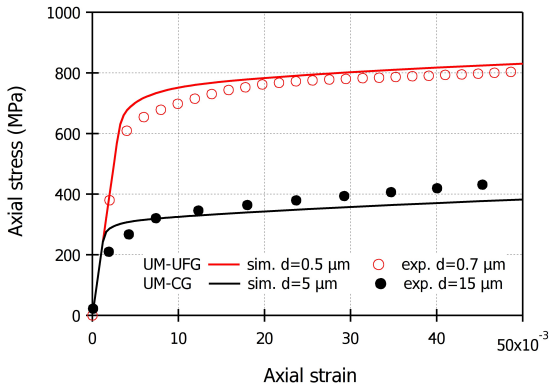

Figure 9: Simulated tensile stress-strain responses of the two unimodal polycrystals with respective mean grain sizes of 0.5 (UFG) and 5 µm (CG). Experimental tensile curves with UFG and CG are also included for comparison purpose.

The axial stress field in the CG unimodal polycrystal is presented in Figure 10 for two imposed strains: $\varepsilon = 0.005$ and $\varepsilon = 0.05$. As the only difference between the UFG and the CG polycrystals stands in the mean grain size - the microstructural morphology is exactly the same -, the UFG polycrystal displays the same stress fields but with larger values due to the grain size strengthening. These stress fields, illustrated in Figures 10(a) and 10(c) for a low and a high imposed strain respectively, exhibit rather homogeneous stress distributions with some localization patterns which could be due to the local grain orientations. This homogenous character of the stress distribution can be also observed in the Probability Density Functions (PDF) illustrated for the UFG and CG samples in Figures 10(b) and 10(d) for $\varepsilon = 0.005$ and $\varepsilon = 0.05$, in the order given. For both grain sizes the stress distributions correspond to lognormal functions with, as expected, larger values for UFG than for CG.

When it comes to the strain, the axial strain field (for the CG case) and corresponding PDF (for both CG and UFG) are displayed in Figure 11 for total strain levels of 0.005 and 0.05. At $\varepsilon = 0.005$, as observed in Figure 11(a), shear bands related to strain localization appear, oriented at 45° with respect to the tensile axis. These shear bands correspond to strain localization patterns which result from the heterogeneous deformation on the meso-scale of the microstructure: they typically expand over few grains, have a width of about one grain or less, and lead to an intensification of the strain with a factor of about 5 to 10 with respect to the imposed strain. These characteristics are in agreement with observations from digital image correlation analyses made in Doumalin et al. (2003); St-Pierre et al. (2008) or from 3D crystal plasticity FE analyses made in Barbe et al. (2009). With an increase in strain to $\varepsilon = 0.05$, the localization bands only exhibit larger strain values whereas their number and shape remain similar (see Figure 11(c)). In terms of PDF, as seen in Figures 11(b) and 11(d), a slight difference exists between the two considered grain sizes at low imposed strain and it vanishes for $\varepsilon = 0.05$.

In order to explain the difference in the strain PDF between the two grain sizes at low total strain, attention has been paid to the activation of plastic slip on the slip systems according to two criteria: one where plasticity is considered to be activated as soon as a slip γ^s exceeds a given

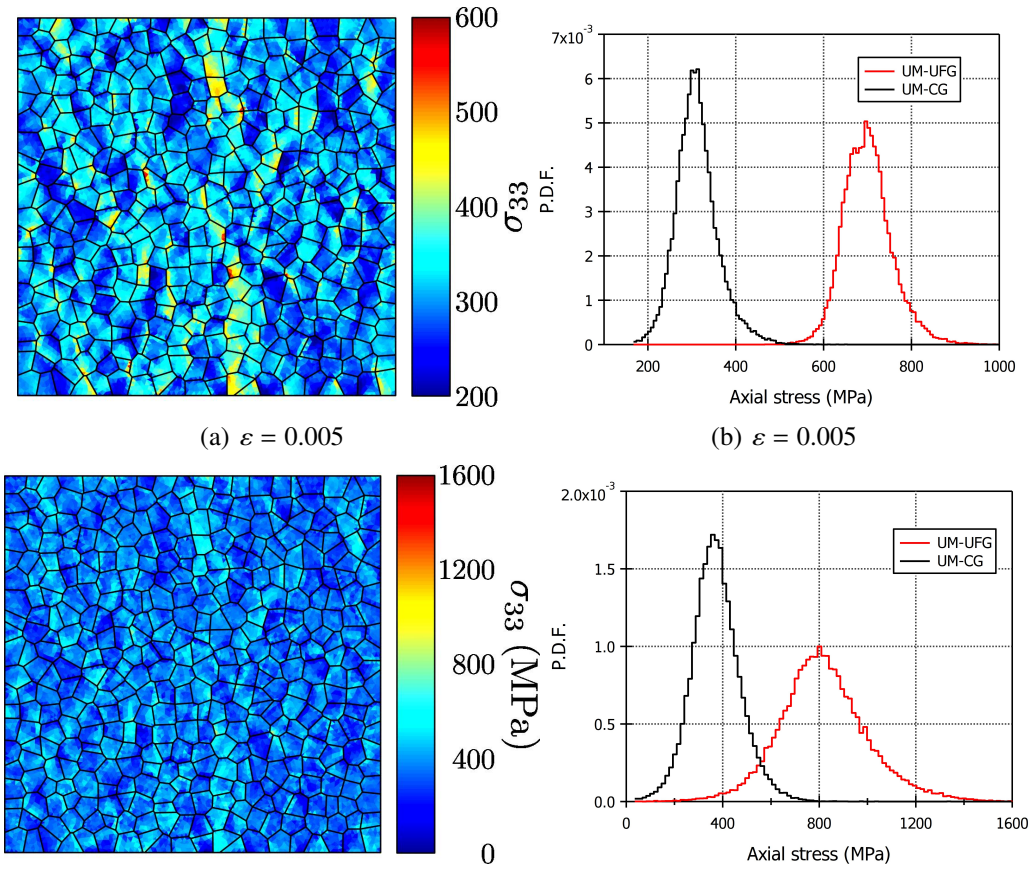

(a) $\varepsilon = 0.005$ (b) $\varepsilon = 0.005$

(c) $\varepsilon = 0.05$ (d) $\varepsilon = 0.05$

Figure 10: Spatial and statistical axial stress distributions in the unimodal CG polycrystals: (a) stress field for $\varepsilon = 0.005$, (b) stress probability density function for $\varepsilon = 0.005$, (c) stress field for $\varepsilon = 0.05$ and (d) stress probability density function for $\varepsilon = 0.005$.

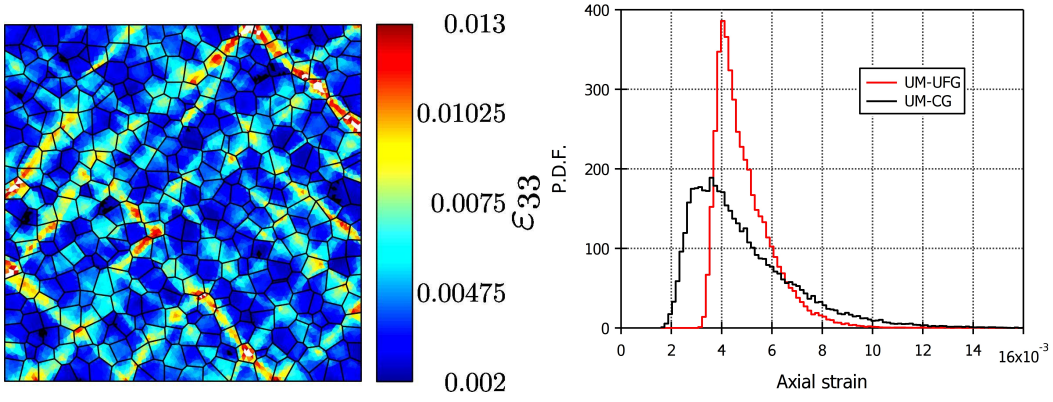

(a) $\varepsilon = 0.005$ (b) $\varepsilon = 0.005$

(c) $\varepsilon = 0.05$ (d) $\varepsilon = 0.05$

Figure 11: Spatial and statistical axial strain distributions in the CG unimodal polycrystal (a) strain field for $\varepsilon = 0.005$ (CG case), (b) strain probability density function for $\varepsilon = 0.005$, (c) strain field for $\varepsilon = 0.05$ (CG case) and (d) strain probability density function for $\varepsilon = 0.005$.

threshold on a system s, the other where it is the slip rate $\dot{\gamma}^s$ which determines the activation. These two criteria are associated to different information about the plastic activity. The first one reports the number of activated slip systems which carry the major part of plastic deformation up to a given total strain. This number is necessarily an increasing function of the strain. The second criterion provides information on the gliding systems at a given total strain, independently to their contributions to the overall plastic deformation. The number of active slip systems may then decrease upon increasing imposed strain. For each criterion, the associated critical value was chosen in order *(i)* to ensure that the number of activated slip systems remains lower than five (the minimal number of active slip systems to realize any strain according to the model of Taylor) and *(ii)* to be related with a realistic strain value at the onset of homogeneous plasticity. For 316L, based on a strain hardening rate analysis, homogeneous plasticity has been reported to occur experimentally for a total strain larger that about 0.01 depending on the grain size (Feaugas and Haddou, 2003). Using this approach, satisfactory results were obtained with thresholds $\gamma_0^s = 0.005$ and $\dot{\gamma}_0^s = 10^{-4}\text{s}^{-1}$, for the shear based and the shear rate based criteria, respectively.

The plasticity activation criteria enable to define whether an integration point is in the elastic or in the plastic regime. Figure 12(a) provides the evolution of the volume fraction of elements in the elastic regime according to the imposed strain, for both criteria. Whatever the criterion, this volume fraction starts to decrease after the elastic regime and tends to zero. According to the shear rate criterion, the imposed strain for which the fully plastic regime is reached in the CG polycrystal is $\varepsilon = 0.005$ and at this strain, the UFG polycrystal still contains a significant part of elements in the elastic regime, which explains the differences between the UFG and CG statistical distributions of Figure 11(b). It can be noted that the onset of full plasticity depends on the criterion. Figure 12(b) shows the evolution upon straining of the mean number of active slip systems over the polycrystals UFG and CG for both activation crieria. Whatever the criterion, this number is lower for UFG than for CG at the beginning of plasticity. While increasing the imposed strain, this difference reduces and reaches approximately 2.7 for both polycrystals and both criteria, which is lower than the remarkable value of 5 in the Taylor model.

5.2. Bimodal polycrystal responses

In order to highlight the influence of the bimodal grain size distribution on the mechanical behavior, the previous analyses on unimodal (UM) polycrystals have been extended to the bimodal (BM) ones. They are presented in the following paragraphs by making comparisons between BM and UM behaviors.

5.2.1. Macroscopic response

Figure 13 illustrates the predicted macroscopic tensile behavior (axial stress versus axial strain) for the two kinds of bimodal microstructures investigated numerically in this study: isolated (BM-iCG) or clustered (BM-clCG) coarse grains (shown in Figures 5(a) and 5(b) respectively). The macroscopic behavior of these bimodal polycrystals (BM-PX) is systematically compared to the

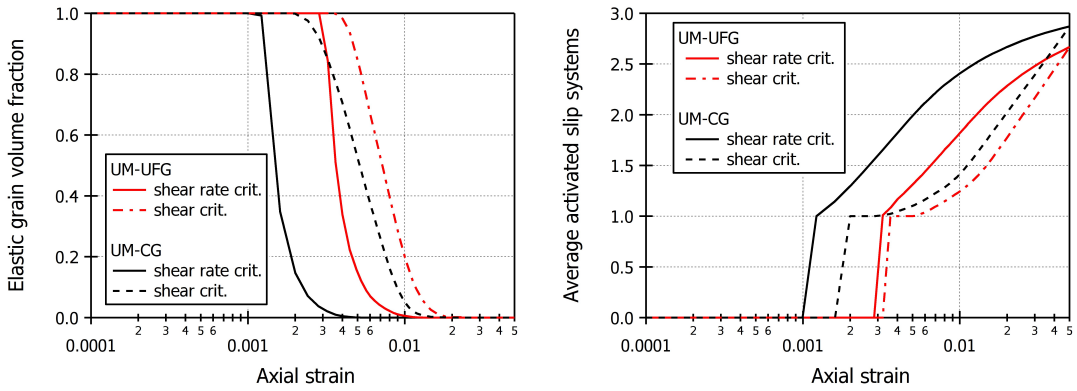

(a) (b)

Figure 12: Plastic activity upon straining in the unimodal polycrystals: (a) volume fraction of elements in the elastic regime and (b) average number of active slip systems over the polycrystals. Both shear based (γ^s) and shear rate based ($\dot{\gamma}^s$) criteria have been used.

mean behavior of each grain population it is made of (i.e. UFG, labelled BM-UFG, and CG, labelled BM-CG) and to the macroscopic behavior of their unimodal counterparts examined in the previous section (called UM-UFG and UM-CG, respectively). For comparison purpose, the experimental tensile curve of the series 1 sample with 75% UFG (experimental sample with the closest bimodal grain size distribution) is also provided in this figure.

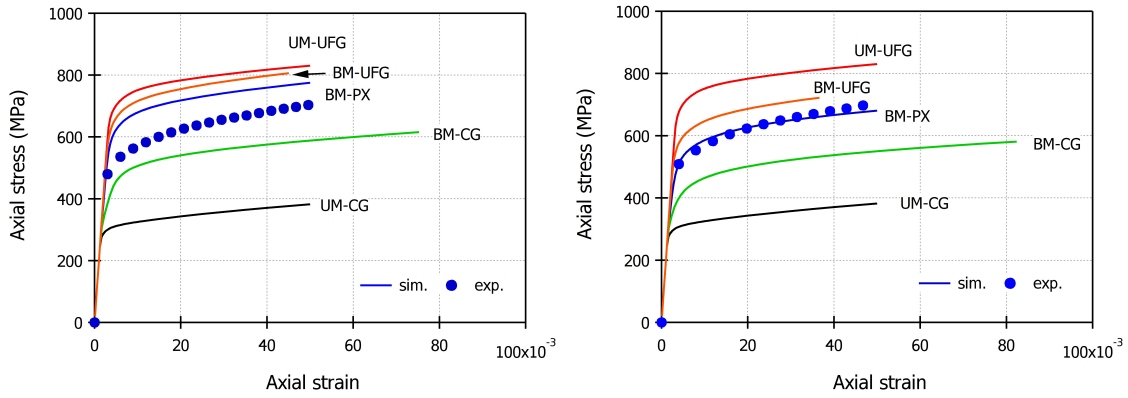

(a) BM-iCG (b) BM-clCG

Figure 13: Simulated average axial stress-strain responses of *(i)* the bimodal polycrystals, *(ii)* each of their grain populations and *(iii)* their corresponding unimodal counterparts for (a) the isolated bimodal case and (b) the clustered bimodal case. Experimental tensile curve of the series 1 sample with 75% UFG is also depicted.

As expected, the curves of the bimodal polycrystals lie between those of the two unimodal UFG and CG. However, the coarse grain spatial distribution inside the polycrystal clearly influences the deviation from the UFG unimodal curve. Indeed, in the case of the isolated CG (Fig. 13(a)), the stress decrease for the bimodal case with respect to the UFG unimodal one is about

50 MPa whereas this value is close to 200 MPa in the case of clustered CG (Fig. 13(b)). It can also be noted that the agreement between the simulations and the experimental tensile curve of series 1 sample with 75% UFG is much better for clustered CG than for isolated ones. Indeed, for this experimental sample, the volume fraction of coarse grains is about 25% which is closer to the BM-clCG polycrystal value (30%) than the BM-iCG one (17%). Moreover, as observed in figure 6(a), the serie 1 experimental sample exhibit CG clusters which correspond to the BM-clCG case.

For both CG configurations in bimodal polycrystals, the extracted stress values for the CG population (BM-CG) is larger than the one of the unimodal counterpart (UM-CG). This increase in axial stress is about 200 MPa and is only slightly affected by the CG positions. For the UFG population inside the bimodal polycrystal (BM-UFG), the axial stress is reduced compared to the UFG unimodal case (UM-UFG). This stress modification for the UFG population is, in absolute value, lower than the CG population one and seems to slightly depend on the deformation. Indeed, an increase in strain tends to reduce the difference in stress between the two UFG curves (i.e. UM-UFG and BM-UFG). Nevertheless, unlike the CG population stress, the UFG population mean stress is strongly influenced by the spatial distribution of the CG: the decrease with respect to the UFG unimodal case is approximately 20 MPa for the BM-iCG and 100 MPa for the BM-clCG. It can also be noted that for both isolated and clustered configurations, for the same imposed strain $\varepsilon = 0.05$, the CG inside the bimodal polycrystal has undergone larger deformation than their unimodal counterparts whereas the opposite trend is observed for UFGs. This strain increase for CG in the bimodal case is slightly higher for the clustered configurations than for the isolated one. Besides, still at $\varepsilon = 0.05$ imposed strain, the CG is the most extensively strained population within bimodal polycrystals. These two figures (Fig. 13(a,b)) clearly highlight the coupling between the two grain populations inside the bimodal polycrystals, which affects the macroscopic responses of each grain population, both in stress and in strain. This coupling is, moreover, dependent on the spatial distribution of the CG.

5.2.2. Stress and strain fields

To better describe the coupling features between the two grain populations inside the bimodal polycrystals, simulated axial stress and strain fields were plotted for different strain levels and for the two CG configurations (isolated and clustered). Figures 14(a,c,e) present the axial stress fields for the isolated configuration and for three different total strains: $\varepsilon = 0.0025$, 0.02 and 0.04 respectively. For each of these imposed strains, the statistical distributions (PDF) of stress within all the grains and in each of its grain populations are plotted in Figures 14(b,d,f). Distributions obtained from the unimodal polycrystals are also plotted to enable comparisons.

At low imposed strain ($\varepsilon = 0.0025$, Fig. 14(a)), clear manifestations of long range interactions between each grain population can be observed. In the UFG population, wide and elongated low stress channels have formed alongside the tensile direction. These channels are controlled by the presence of CG and are clearly observed on the PDF associated with the stress field (Fig. 14(b)). Indeed, the UFG population inside the bimodal polycrystal exhibits a stress distribution (orange line) with a larger spread towards low stress values compared to the unimodal UFG case (red line).

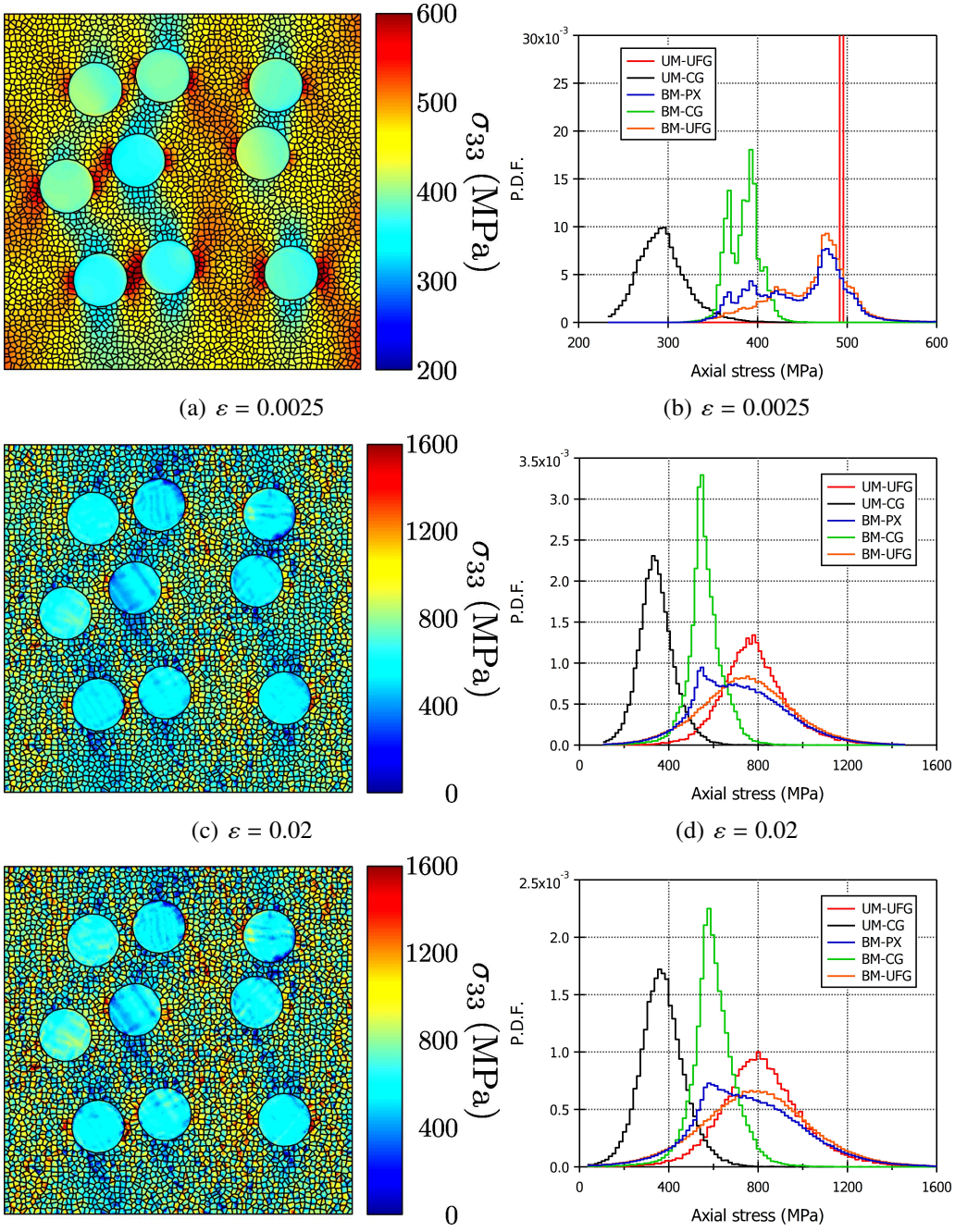

(a) $\varepsilon = 0.0025$ (b) $\varepsilon = 0.0025$

(c) $\varepsilon = 0.02$ (d) $\varepsilon = 0.02$

(e) $\varepsilon = 0.04$ (f) $\varepsilon = 0.04$

Figure 14: Axial stress in the isolated bimodal configuration at three levels of imposed strain ($\varepsilon = 0.0025$, 0.02 and 0.04): spatial distribution in (a,c,e) and statistical distribution in (b,d,f). On the stress field contours, the tensile direction is vertical.

On the contrary, as already observed on the macroscopic tensile curves, the stress distribution for the CG population inside the bimodal polycrystal (BM-CG, green line) is shifted towards higher stress values with respect to the CG unimodal polycrystal (UM-CG, black line). One may also note that the presence of the CG has induced an increase of the axial stress in the UFG located in the close neighboring of their equators, as has been characterized in bimodal polycrystals with a single central CG (Barbe et al. (2020); Flipon et al. (2020)).

With an increase in total strain, those low stress channels are less marked in the stress fields (Fig. 14(c,e)). At $\varepsilon = 0.02$, the PDF of axial stress for the UFG population inside the BM polycrystal (BM-UFG, orange line, Fig. 14(d)) is close to the UFG unimodal polycrystal (red line) with, yet, higher probabilities for low stresses related to the low stress channels. This difference between the two UFG curves (i.e. BM-UFG and UM-UFG) is reduced at $\varepsilon = 0.04$. For the CG population inside the bimodal polycrystal, contrary to the UFG, it seems that their PDF are only shifted towards higher stress values without any modification in shape. This shift does not depend on the strain. Furthermore, it appears that the difference in PDF between the two grain populations inside the bimodal polycrystal reduces upon tension at the early stage of straining, suggesting a process of uniformization in the responses of grains in the bimodal polycrystal.

For the same imposed strain levels, the axial strain fields and corresponding PDF are plotted in Figure 15 for the same configuration of isolated CG. At low strain ($\varepsilon = 0.0025$, Fig. 15(a)), CG carry most of the deformation whereas low strain channels, similar to the stress ones, have formed in the UFG matrix. The corresponding PDF, in Figure 15(b), confirms this feature with a strain distribution shifted towards higher and lower values compared to the unimodal counterparts for the CG and UFG populations respectively.

With an increase in imposed strain, the low strain channels observed in the UFG population for $\varepsilon = 0.0025$ are no longer visible and localization bands oriented at 45° with respect to the tensile direction have developped (Fig. 15(c,e)). Unlike conventional unimodal materials which exhibit - see previous section - randomly distributed shear bands, for bimodal polycrystals, all localization bands intersect the coarse grains at which plastic strain initiated at the beginning of plasticity. In the PDF (Figures 15(d) and 15(f) for $\varepsilon = 0.02$ and 0.04 respectively), as localization bands developed both in coarse grains and in the matrix of fine grains, only slight differences can be observed between the distributions within the respective grain populations in bimodal or unimodal polycrystals.

For the clustered CG case, the axial stress fields and corresponding PDF are plotted in Figure 16 whereas the axial strain fields and related PDF are shown in Figure 17. Concerning the stress fields, Figures 16(a), 16(b) and 16(c) reveal the developpement of low stress channels as the imposed strain increases, similarly to what the isolated case of CG exhibits. The main distinction which can be made in the axial stress fields of the isolated and clustered cases concerns its statistical distribution within the UFG population: in the clustered case, the presence of coarse grains within the polycrystal (BM-UFG orange line to compare with the UM-UFG red line) not only causes a spread of the distribution towards lower and higher values - as in the isolated case

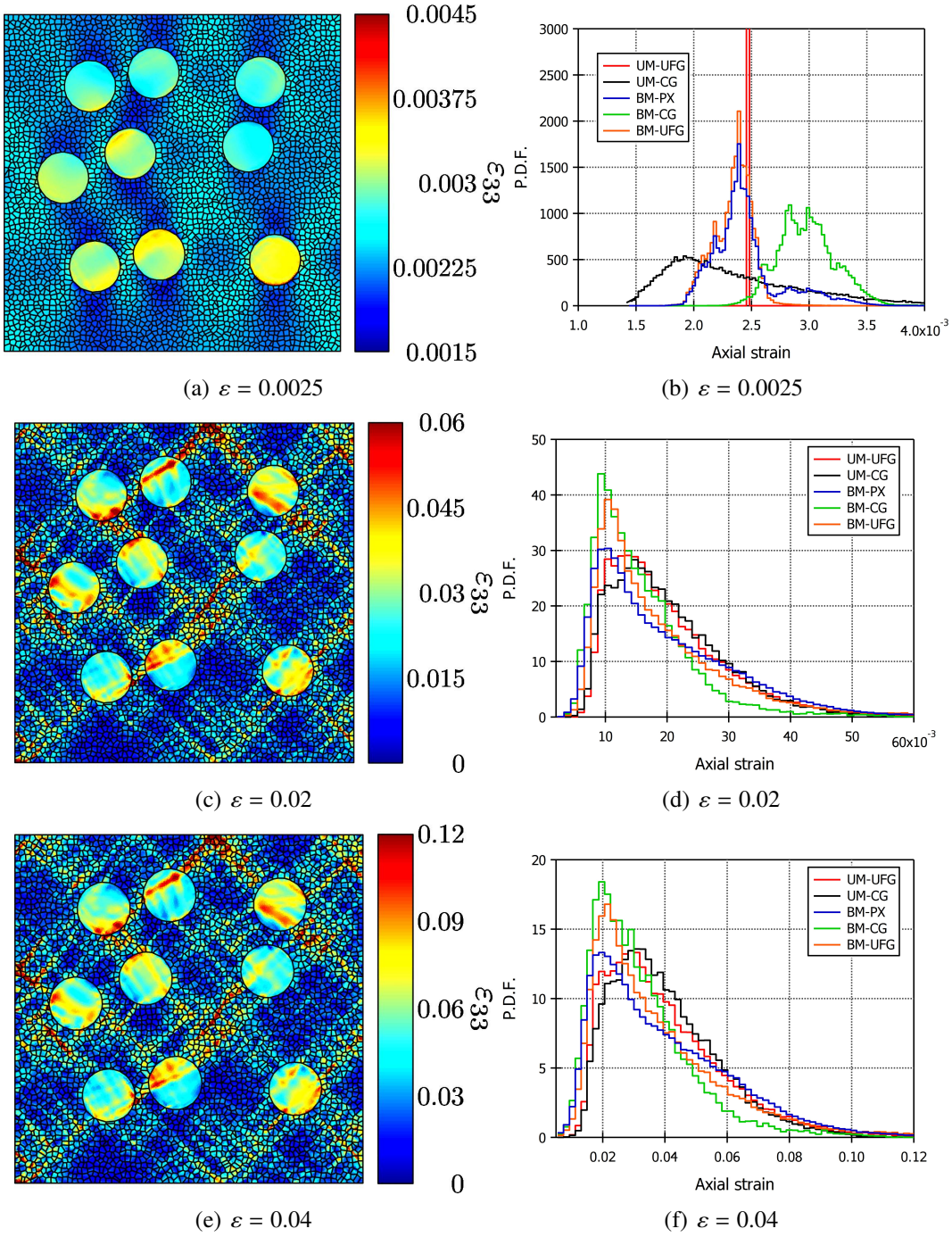

(a) $\varepsilon = 0.0025$ (b) $\varepsilon = 0.0025$

(c) $\varepsilon = 0.02$ (d) $\varepsilon = 0.02$

(e) $\varepsilon = 0.04$ (f) $\varepsilon = 0.04$

Figure 15: Axial strain in the isolated bimodal configuration at three levels of imposed strain ($\varepsilon = 0.0025$, 0.02 and 0.04): spatial distribution in (a,c,e) and statistical distribution in (b,d,f). On the strain field contours, the tensile direction is vertical.

-, it also shifts the maximal probability towards a lower value. This indicates a stronger coupling between grain populations if coarse grains are clustered.

Dealing with strain fields, Figures 17(a), 17(b) and 17(c), respectively for imposed strains ε = 0.0025, 0.02 and 0.04, highlight that the presence of CG clusters causes the occurrence of a single major localization band at approximately 45° with respect to the tensile direction, whereas there were several of them in the case of isolated CG. The position and the orientation of this band seems to be primarily correlated with the direction of the highest linear density of coarse grains within the polycrystal. As seen from the statistical distributions in Figures 17(b), 17(d) and 17(e), the formation of this dominant deformation band tends to exacerbate the deviation of the local strains in a bimodal immerged grain population from those occuring within their unimodal counterpart.

Based on these stress and strain fields analyses, it is clear that the effects of coupling two grain size populations within a polycrystal are maximal at the onset of plasticity. It is indeed the moment when channels of low stress and strain develop in the UFG matrix and when stress-strain responses of bimodal immerged grains depart most from those of unimodal immerged grains. Once plasticity is established, localization bands intensify and stress gradually tends to a uniformization but distinctions between the unimodal and the bimodal configuration remain clear. However, these features strongly depend on the spatial distribution of the coarse grains.

5.2.3. Slip systems activation

To understand the origin of the stress and strain modifications in the UFG and CG populations in the bimodal polycrystals compared to their unimodal counterparts, plasticity activation and number of activated slip systems were investigated as a function of the total strain. Figure 18 represents the evolution of the elastic volume fraction within polycrystals as the imposed strain increases. Each plasticity activation criterion is used to compute this volume fraction: the shear criterion γ^s (Fig. 18(a,c)) and the shear rate criterion $\dot{\gamma}^s$ (Fig. 18(b,d)). Figure 18(a,b) concern the isolated configuration BM-iCG and Figure 18(c,d) concern the clustered configuration BM-clCG. Each grain size population is considered in its unimodal and bimodal configuration.

It can first be observed that the coarse grains reach the fully plastic regime for a lower imposed strain in the bimodal configuration than in the unimodal configuration, whatever the criterion and the spatial distribution of CG. Secondly, an opposite trend is observed for UFG which get fully plastic for larger total strains in the bimodal case. This trend does not depend on the activation criterion but strongly depends on the isolated or clustered configuration (comparison of Figures 18(a) and 18(b)). For the clustered configuration, the critical total strain at which the UFG population is fully plastified (γ^s criterion) is about 0.04 versus 0.03 for the isolated configuration and 0.02 for the unimodal polycrystal. According to the shear rate criterion, the volume fraction of elastic elements in the bimodal polycrystals reach a plateau at an imposed strain of 0.0025 approximately. In the strain range of these plateaus, BM-CG are fully plastified whereas BM-UFG still behave elastically, corresponding to the well-known stage II of the behavior of composite materials (Lin

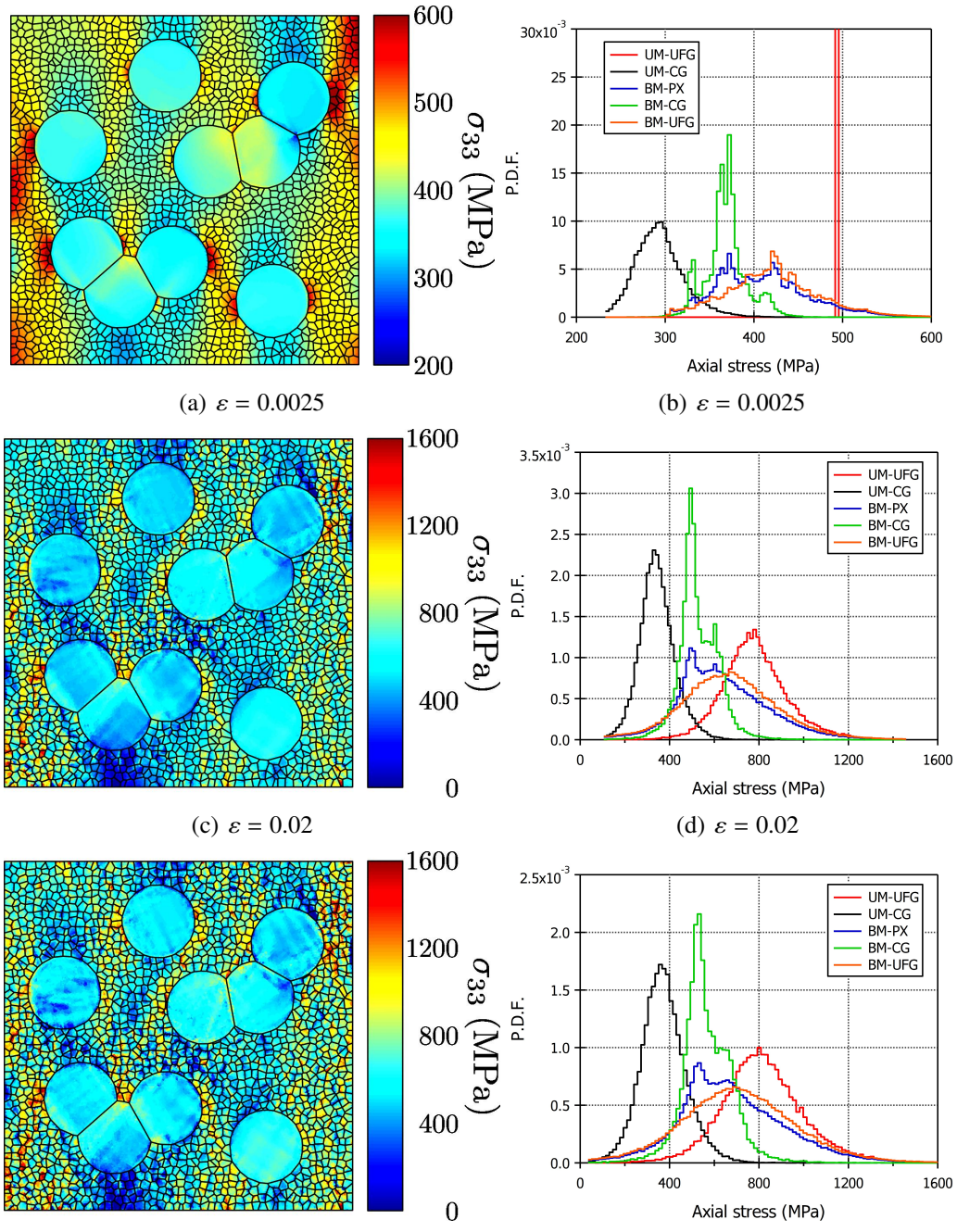

(a) $\varepsilon = 0.0025$ (b) $\varepsilon = 0.0025$

(c) $\varepsilon = 0.02$ (d) $\varepsilon = 0.02$

(e) $\varepsilon = 0.04$ (f) $\varepsilon = 0.04$

Figure 16: Axial stress in the clustered bimodal configuration at three levels of imposed strain ($\varepsilon = 0.0025$, 0.02 and 0.04): spatial distribution in (a,c,e) and statistical distribution in (b,d,f). On the stress field contours, the tensile direction is vertical.

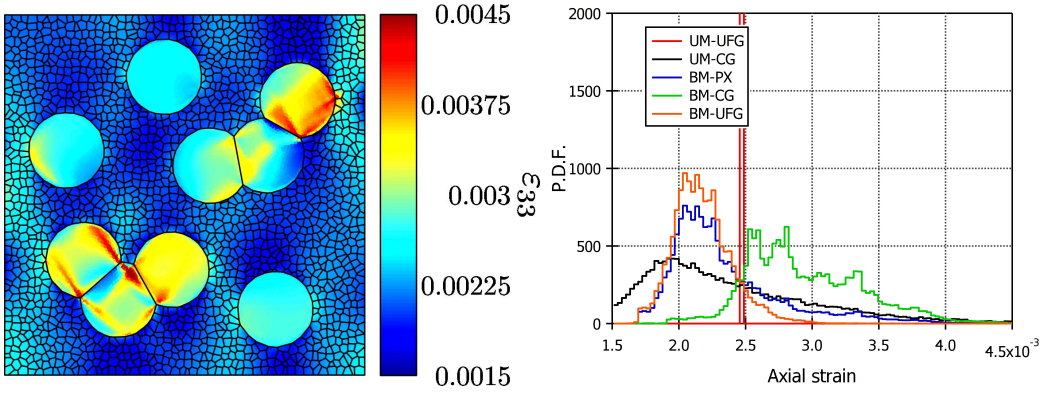

(a) $\varepsilon = 0.0025$ (b) $\varepsilon = 0.0025$

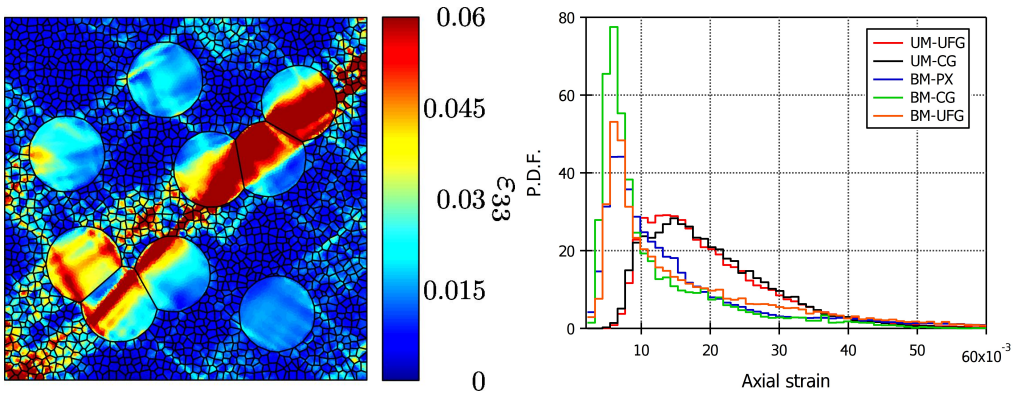

(c) $\varepsilon = 0.02$ (d) $\varepsilon = 0.02$

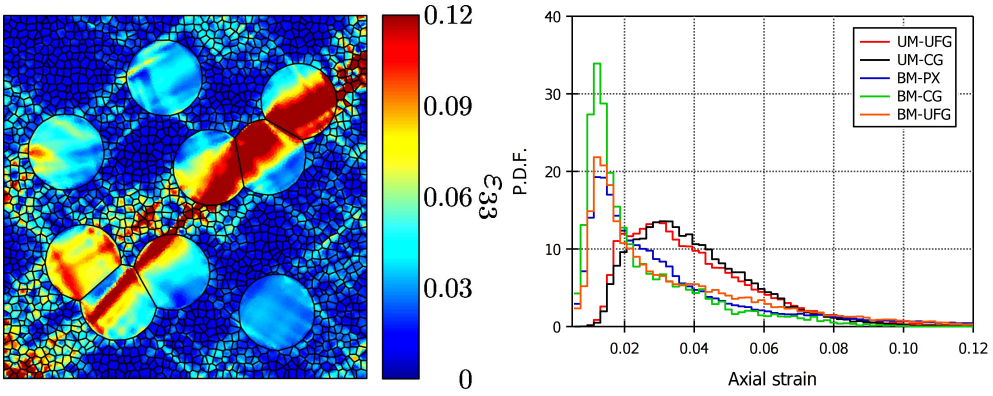

(e) $\varepsilon = 0.04$ (f) $\varepsilon = 0.04$

Figure 17: Axial strain in the clustered bimodal configuration at three levels of imposed strain ($\varepsilon = 0.0025$, 0.02 and 0.04): spatial distribution in (a,c,e) and statistical distribution in (b,d,f). On the strain field contours, the tensile direction is vertical.

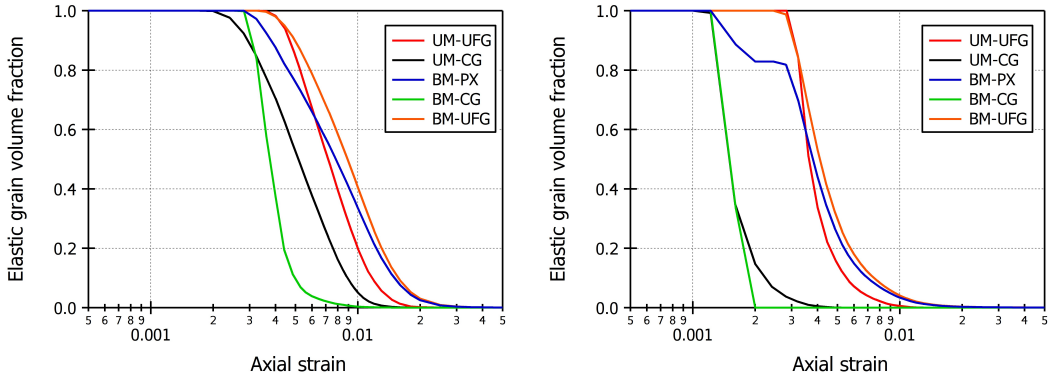

(a) BM-iCG, γ^s criterion

(b) BM-iCG, $\dot{\gamma}^s$ criterion

(c) BM-clCG, γ^s criterion

(d) BM-clCG, $\dot{\gamma}^s$ criterion

Figure 18: Evolution of the volume fraction of elastic elements as a function of the imposed strain: (a) isolated configuration, γ^s criterion, (b) isolated configuration, $\dot{\gamma}^s$ criterion, (c) clustered configuration, γ^s criterion and (d) clustered configuration, $\dot{\gamma}^s$ criterion.

et al., 1992; Sawicki, 1983).

The analyses made from Figure 18 are extended to the mean number of activated slip systems in Figure 19. The presentation of results according to the employed activation criterion or to the considered bimodal polycrystal is organised in the same way as in Figure 18.

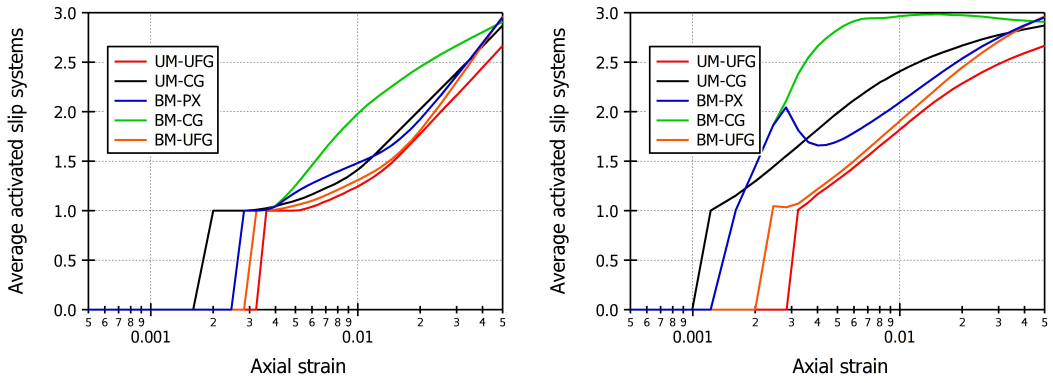

(a) BM-iCG - γ^s criterion

(b) BM-iCG - $\dot{\gamma}^s$ criterion

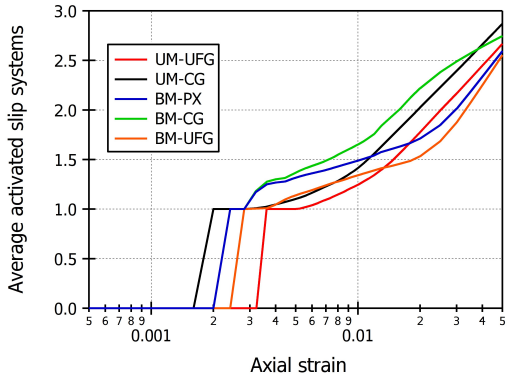

(c) BM-clCG - γ^s criterion

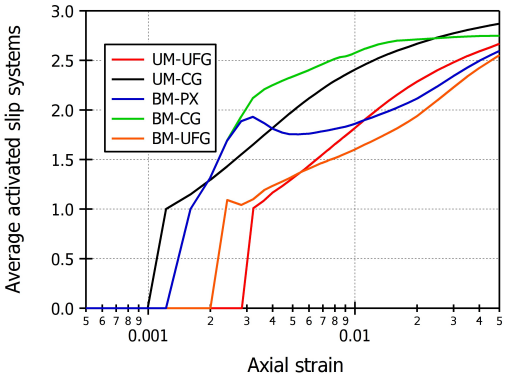

(d) BM-clCG - $\dot{\gamma}^s$ criterion

Figure 19: Evolution of the average number of activated slip systems as a function of the imposed strain: (a) isolated configuration, γ^s criterion, isolated configuration, $\dot{\gamma}^s$ criterion, (c) clustered configuration, γ^s criterion and (d) clustered configuration, $\dot{\gamma}^s$ criterion.

For the CG population, using both plastic activation criteria, the simulations reveal that the increase in the number of activated slip systems upon straining is larger in the bimodal case than in the unimodal one. This trend is however dependent on the spatial distribution of coarse grains. For isolated CG (Fig. 19(a,b)), this increase with respect to the unimodal case is much larger than for the clustered configuration (Fig. 19(c,d)). At $\varepsilon = 0.05$, the average value of activated slip systems in the coarse grains is about 2.6 for both kinds of bimodal polycrystal (i.e. BM-iCG or BM-clCG) and both activation criteria. It is further noticed that, according to the $\dot{\gamma}^s$ criterion, the maximal number of activated slip systems is reached for a total strain of 0.015 and remains almost constant for larger strains whereas a continuous increase is observed in the unimodal case. Concerning the UFG population, for the isolated configuration, the evolution of the number of activated slip systems is similar for the two criteria with a slightly higher value at $\varepsilon = 0.05$ for the bimodal case compared to the unimodal one. However, for the clustered configuration, the bimodal grain size distribution clearly decreases the number of activated slip systems compared to the unimodal counterpart.

To understand the role played by the spatial distribution of CG on the plastic activity of the UFG population, fields contours of the number of activated slip system are considered in Figure 20 for the isolated configuration, for the two plastic activation criteria and four total strain levels: $\varepsilon = 0.0025$, 0.01, 0.02 and 0.04. For the lowest strain level (Fig. 20(a,b)), only the coarse grains exhibit plastic activity (case of shear rate criterion) whereas the UFG still behave elastically, in agreement with Figures 18(a) and 18(b). With an increase in strain, plasticity develops in the UFG matrix in a heterogeneous way. As illustrated for $\varepsilon = 0.01$ in Figures 20(c) and 20(d), plastically deformed UFG are located in bands which seem to be similar to the shear deformation ones illustrated in Figure 14. For this strain level, the volume fraction of elastic elements contained in those bands is much lower according to the $\dot{\gamma}^s$ criterion than according to the γ^s one. As the imposed strain is increased (Figures 20(d) to 20(g)), plasticity tends to homogenize over the two grain populations.

Analyses made from contour plots of Figure 20 in the case of isolated CG are extended to the case of clustered CG in Figure 21. The elastic/plastic behavior of each grain population is similar to the one reported for the isolated configuration. However, as compared to the previous case, for $\varepsilon = 0.01$ (Fig. 21(c,d)) and $\varepsilon = 0.02$ (Fig. 21(c,d)), the volume fraction of plastically deforming UFG is greatly reduced. As for the isolated configuration, the increase in total strain reduces the volume fraction of elastic UFG, which are expected to be fully plastic for strain levels above 0.03 according to Figure 18.

The bimodal grain size distribution induces, hence, a delay of the onset of plastic activity in the UFG matrix compared to its unimodal counterpart. For a given imposed strain, the volume fraction of UFG remaining in the elastic regime depends on the considered plasticity activation criterion and also on the spatial distribution of coarse grains.

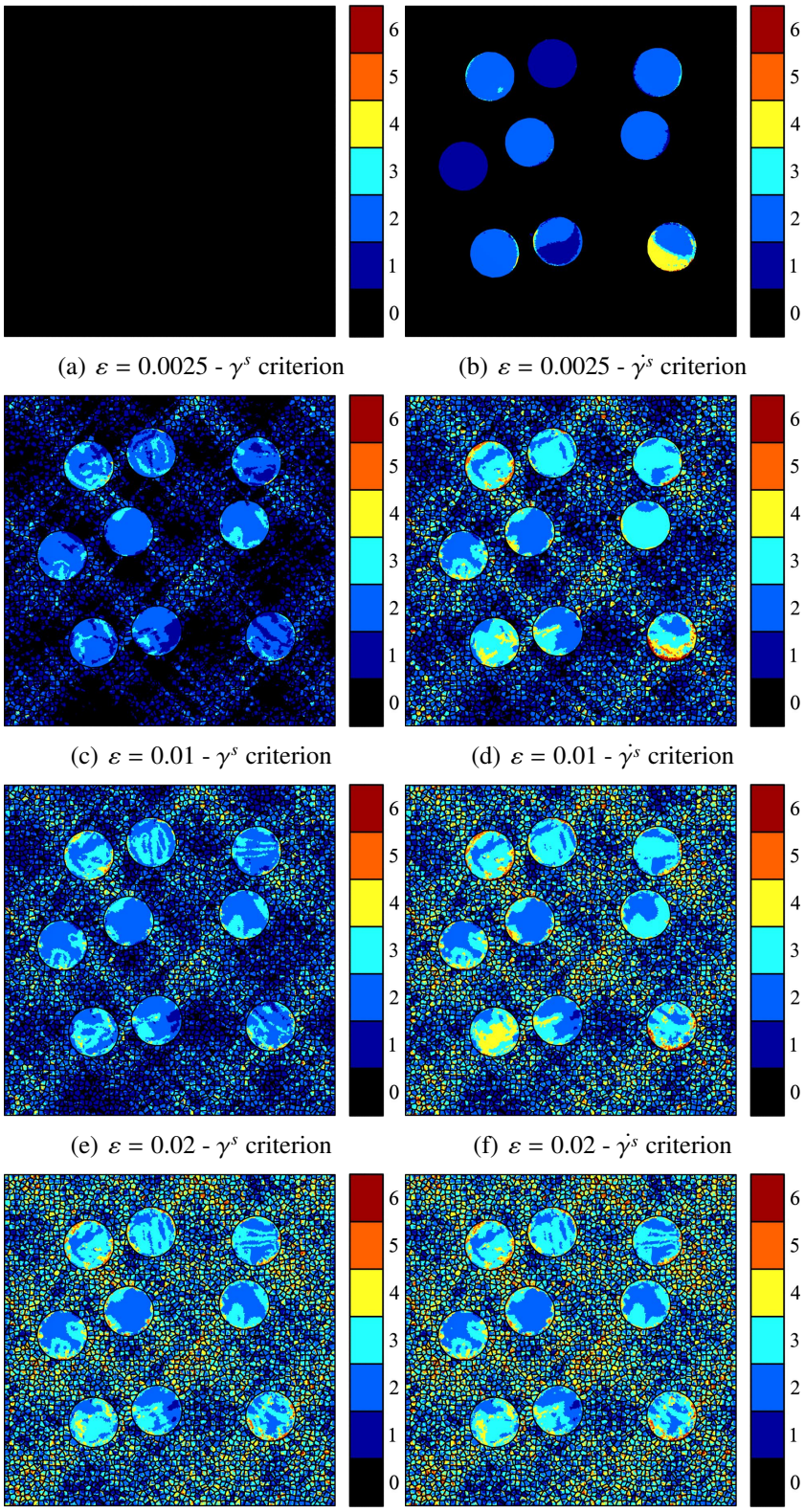

(a) $\varepsilon = 0.0025$ - γ^s criterion (b) $\varepsilon = 0.0025$ - $\dot{\gamma}^s$ criterion

(c) $\varepsilon = 0.01$ - γ^s criterion (d) $\varepsilon = 0.01$ - $\dot{\gamma}^s$ criterion

(e) $\varepsilon = 0.02$ - γ^s criterion (f) $\varepsilon = 0.02$ - $\dot{\gamma}^s$ criterion

(g) $\varepsilon = 0.04$ - γ^s criterion (h) $\varepsilon = 0.04$ - $\dot{\gamma}^s$ criterion

Figure 20: Spatial distribution of the number of activated slip systems in the clustered CG configuration, at four imposed strains: $\varepsilon = 0.0025, 0.01, 0.02, 0.04$, from top to bottom. Left and right columns correspond to the shear criterion γ^s and the shear rate activation criterion $\dot{\gamma}^s$. The tensile direction is vertical.

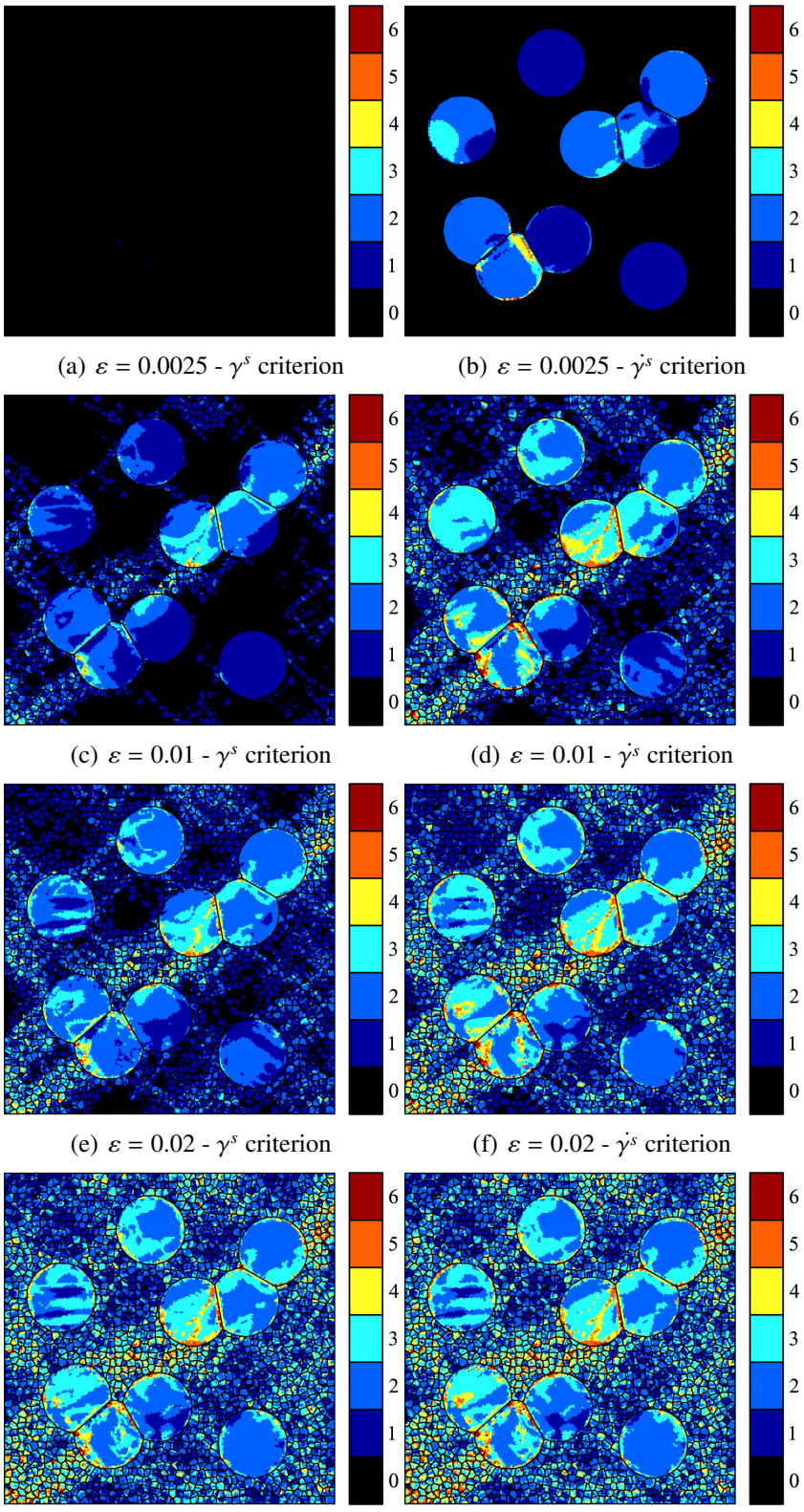

(a) $\varepsilon = 0.0025$ - γ^s criterion (b) $\varepsilon = 0.0025$ - $\dot{\gamma}^s$ criterion

(c) $\varepsilon = 0.01$ - γ^s criterion (d) $\varepsilon = 0.01$ - $\dot{\gamma}^s$ criterion

(e) $\varepsilon = 0.02$ - γ^s criterion (f) $\varepsilon = 0.02$ - $\dot{\gamma}^s$ criterion

(g) $\varepsilon = 0.04$ - γ^s criterion (h) $\varepsilon = 0.04$ - $\dot{\gamma}^s$ criterion

Figure 21: Spatial distribution of the number of activated slip systems in the clustered CG configuration, at four imposed strains: $\varepsilon = 0.0025, 0.01, 0.02, 0.04$, from top to bottom. Left and right columns correspond to the shear criterion γ^s and the shear rate activation criterion $\dot{\gamma}^s$. The tensile direction is vertical.

6. Discussion

The different results described in the previous paragraphs, based both on experiments and numerical modeling, clearly revealed the impact of the two grain populations on the mechanical properties. In the following paragraphs, those results are discussed in terms of grain population interactions, intergranular backstress and grain size ratio between the two grain populations.

6.1. Grain population interactions

Crystal plasticity simulations explicitely highlight the effect of the ultra-fine grains on the behavior of coarse grains and vice versa. Strong interactions arise between the two grain populations, affecting the constitutive behavior at both the macroscale of a grain population and the local scale of grains.

Concerning coarse grains, Figures 13 and 14 exhibit, first, that CG are more constrained in the bimodal configuration than in the unimodal one. This phenomenon arises from the high plastic strain incompatibilities between UFG and CG, which increase in turn the stresses in the CG population. A distinction can then be made according to the CG spatial distribution: if CG are isolated as single inclusions within the matrix of UFG, the observed effect is more pronounced than if CG are clustered, in direct relation with the nature of the neighborhood of the CG.

However, in both bimodal configurations, the axial stress difference between the BM-CG population and its unimodal counterpart (UM-CG) tends to increase for axial strain up to about 0.01 and 0.02 for the isolated and clustered configuration respectively. These two critical axial strain levels correspond to the stabilization of the number of active slip systems onto a plateau according to the shear rate criterion (Fig. 19(b,d)). As compared to the unimodal case, this mean number of active slip systems is greatly increased in the CG of the bimodal polycrystals, because of the larger strain incompatibilities they encounter as they interact with UFG. As soon as these incompatibilites are accommodated, the number of active slip systems in the CG population remains constant and the difference in mean behavior between the CG population and its unimodal counterpart stops increasing.

In the isolated configuration and at low total strain (Fig. 14(a,b)), the high strain incompatibilities between UFG and CG also give rise to a twofold stress distribution in the CG. In the vicinity of the grain boundaries, the stress level is higher than in the core region, due to the maximal strain incompatibilities at low plastic strain. As the total strain is increased, this particular stress distribution is no longer observed. In the clustered configuration, as neighboring CG may have specific misorientations which cause strain incompatibilities, the twofold stress distribution remains always visible, even at moderate strain levels ($\varepsilon = 0.04$, Fig. 16(f)).

The increase in strain incompatibilites with the neighboring grains for the CG in the bimodal configurations also modifies the plastic activity of this grain population. As observed in Figure 18, in both isolated and clustered configurations, the CG reach the plastic regime at a lower imposed strain in the bimodal configuration than in the unimodal one. Consequently, for low imposed

strain, the CG population exhibits larger strain values in the bimodal configuration than in the unimodal one (Fig. 14 and 16 for BM-iCG and BM-clCG resp.).

This enhanced strain of the BM-CG at low imposed strain induces in turn a modification of the behavior of the UFG population. As observed in Figure 15 (BM-iCG) and Figure 17 (BM-clCG) for an imposed strain $\varepsilon = 0.0025$, the axial strain is reduced in the UFG population resulting in low strain channels ended by CG, along the tensile direction. For this low imposed strain, considering the shear rate criterion (more appropriate for low total strain), CG have already entered the plastic regime whereas UFG remain elastic (Figures 20 and 21, for BM-iCG and BM-clCG respectively). Due to the lower axial strain standing in the UFG of the channels, the stress level is also decreased (Figures 14 and 16 for BM-iCG and BM-clCG respectively), which will also delay the activation of their plastic activity (Fig. 18).

The axial strain contrast between the two grain populations also promotes the formation of shear bands developping from the CG. Whereas unimodal polycrystals display 45 ° oriented shear bands at separate uniformally distributed locations, the shear bands systematically include all CG in the isolated bimodal configuration (Fig. 15). In the clustered configuration, a unique shear band develops alongside with the CG clusters (Fig. 17). This shear band formation in bimodal polycrystals will trigger, in turn, the activation of plasticity in the UFG population as disclosed in Figures 20 and 21.

This combined effect of the initial low strain channel and shear band formation will favor the persistence of the low axial stress channels mentioned in the previous paragraphs, up to high total strains. Nevertheless, in the isolated configuration, as observed in Figure 14, the formation of multiple shear bands which include both UFG and CG tends to reduce the contrast in the behaviors of the grain populations for larger strains. This homogeneization of the behavior is less pronounced in the clustered configuration because of the almost unique shear band involving fewer UFG (Fig. 16) than in the isolated case.

As seen from the stress fields in both bimodal polycrystals, inside the low stress channels, the axial stress does not seem to strongly depend on the total strain, revealing a low strain hardening of the UFG in these regions. To investigate the strain hardening behavior of these grains, the individual responses of three different grains located inside low stress channels of the CG-clustered polycrystal are compared to the responses of three other grains located outside these channels. Figure 22(a) presents the locations of these selected grains in correlation with the stress field, at the imposed strain $\varepsilon = 0.02$. They are labelled A, B, C inside the low stress channels and D, E, F outside. Their respective tensile stress-strain curves are plotted in Figure 22(b).

Outside the low stress channels (grains D,E,F), the tensile responses of the grains are representative of what a grain may undergo within the unimodal UFG polycrystal (Fig. 9): the yield stress is about 600 MPa and after yielding individual responses follow different paths according to the crystallographic orientation and to the neighboring grains. The observed dispersion of the mean stress-strain responses of these grains are similar to those observed in a 3D unimodal poly-

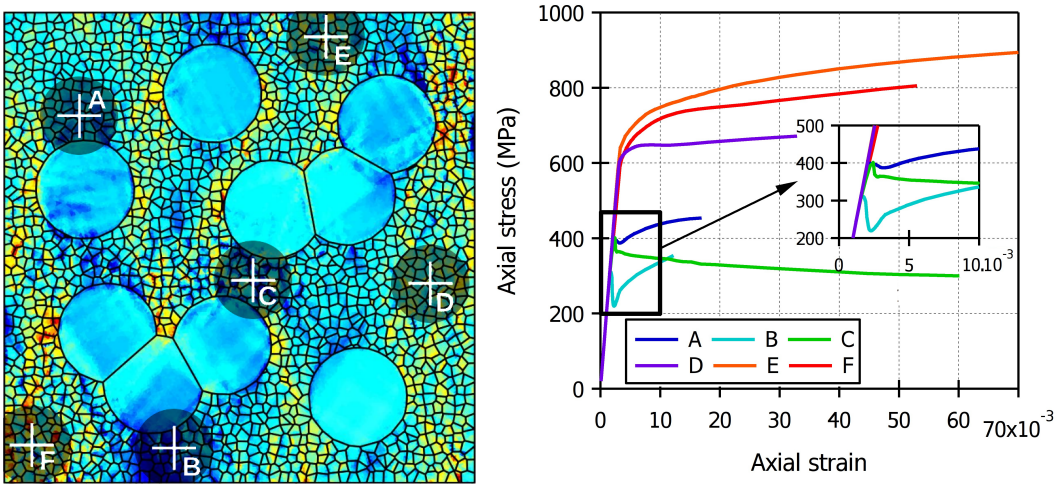

(a) (b)

Figure 22: (a) Locations of six grains selected inside (A, B, C) and outside (D, E, F) the low stress channels of the CG-clustered polycrystal and (b) corresponding tensile stress-strain curves.

crystal (Barbe et al., 2003; N'Guyen et al., 2012).

Inside the low stress channels (grains A,B,C), the axial stress is strongly modified. Firstly, the yield stress is reduced by a factor 2 as compared to the grains D, E and F. Secondly, as seen from the inset, a sudden flow stress decrease is observed for axial strains ranging from 0.001 to 0.0025. According to previously exposed results, this strain range corresponds to the activation of the plasticity in the CG of the bimodal clustered polycrystal. After the plastic regime is established, grains A and B strain harden but grain C softens. Grain C is actually the only one among the three which is located inside the main shear band of the polycrystal and it correspondingly undergoes a much larger strain than any other grain. Concerning grains A and B, we observe on the contrary that their strains are significantly lower than any other grain. Hence, from this observation of different stress-strain behaviors of grains which are all located inside low stress channels, it can be concluded that the strain localization does not influence the formation and further evolution of the low stress channels in the UFG matrix. These channels develop during the yielding of the neighboring CG and they are not affected by the development of shear bands upon loading.

6.2. Intergranular Backstress

The previous section has demonstrated that the interplay between two populations of grains with two different mean grain sizes is the source of strong modifications at the local and global scale of a polycrystal with respect to a conventional polycrystal with a unimodal grain size distribution. These modifications, made from numerical analyses, are in agreement with the tensile properties of bimodal samples characterized experimentally. Indeed, the loading-relaxation-unloading experimental tests carried out for series 2 has revealed that the backstress is the main flow stress level component affected by the bimodal distribution (Fig. 8(e)). In that case, a large decrease in

backstress along with a decrease in CG volume fraction has been characterized, and in the meantime the effective stress was only slightly increased. Following the works of (Feaugas and Haddou, 2003; Keller et al., 2011), in order to better understand the influence of the bimodal grain size distribution on the different flow stress components, a Hall-Petch relationship plot is represented in Figure 23 for the backstress, athermal effective stress and thermally activated effective stress for both unimodal (series 0) and bimodal (series 2) samples. For both cases, a mean grain size is employed, taken from EBSD analyses of all the samples. Two total strain levels are considered: $\varepsilon = 0.003$ in Figure 23(a) and $\varepsilon = 0.03$ in Figure 23(b).

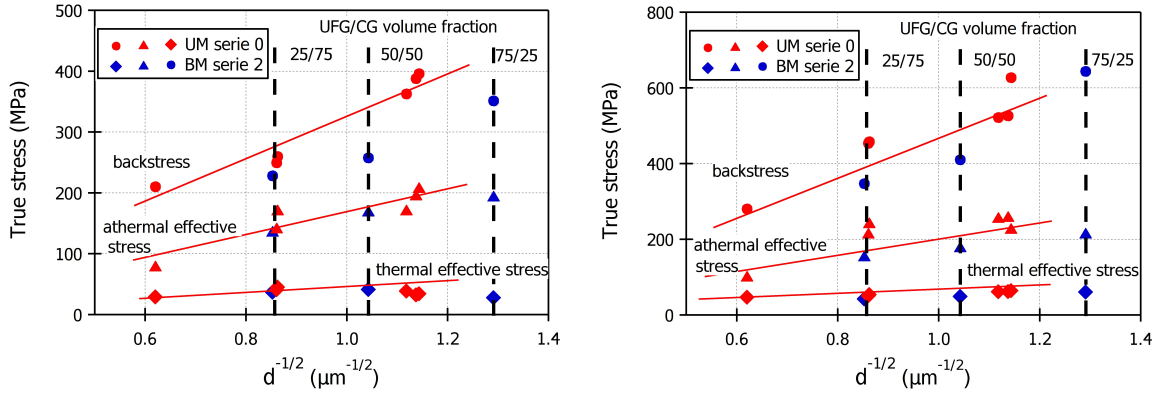

(a) ε=0.003 (b) ε=0.03

Figure 23: Hall-Petch relationship applied to the different flow stress components (backstress, athermal effective stress and thermally activated effective stress) for two imposed strains: (a) $\varepsilon = 0.003$ and (b) $\varepsilon = 0.03$.

At a low strain level corresponding to the onset of plasticity (Fig. 23(a)), for the unimodal samples, the grain size dependence of the three stress components can be well reproduced with the Hall-Petch formalism as already reported for the same alloy elaborated by casting (Feaugas and Haddou, 2003). In agreement with these literature results, the slope is higher for the backstress than for the athermal effective stress. In the case of the thermally activated effective stress, the grain size dependence is negligible. For the bimodal samples (series 2), three pairs of volume fractions in the combination UFG/CG are studied: 25/75, 50/50 and 75/25%. Considering them in the same Hall-Petch plot, *i.e.* being characterized by a single mean grain size, it appears that their backstress components are significanlty smaller than the one expected for a unimodal sample with the same mean grain size.

Using the Hall-Petch formalism, the dependence of the backstress X to the mean grain size d can be formulated using equation 4:

$$X = X_0 + \frac{k_X}{\sqrt{d}} \tag{4}$$

where X_0 is the Y-intercept and k_X is the slope of the Hall-Petch plot.

Following the articles (Feaugas and Haddou, 2003; Keller et al., 2011), X_0 is, to a first approximation, equal to the intragranular part of the backstress associated with the interaction of mobile dislocations with crystalline defects such as incoherent precipitates or heterogeneous dislocation structures. The second term on the right hand side of the equation is then related to the intergranular backstress. This latter is associated to the strain incompatibilites between grains due to their differences in shapes and crystal orientations. Figure 23(a) illustrates that only the intergranular part of the backstress - related to the Hall-Petch slope - is affected by the grain size distribution.

Regarding the effective stress components - athermal and thermally activated -, no significant difference appears between the unimodal and bimodal samples. These stress components are thus independent of the grain size distribution. The low stress channels predicted from crystal plasticity modeling are then expected to be associated with the backstress component at the onset of plasticity.

With an increase in imposed strain to $\varepsilon = 0.03$ (Fig. 23(b)), the differences in backstress components between the unimodal and bimodal samples tend to disappear. For a given mean grain size, the dependence of each flow stress component to the mean grain size is similar whatever the grain size distribution. This result is consistent with the observation, from the previously exposed numerical analyses, of a homogenization process of the mechanical behavior upon loading. The effect of the grain size distribution on the interactions taking place between grains of a polycrystal, especially longer-range ones - associated to the intergranular backstress - can then be said to be maximal at the early stages of plastic strains.

These results reveal, from both experimental and numerical analyses, that embedding coarse grains within a matrix of ultra-fine grains promotes a delay in the activation of plasticity in the ultra-fine-grained matrix and the development of low stress channels. Inside these channels, the intergranular backstress is reduced, which in turn depresses stress concentrations at the interfaces between grains. Both features contribute to an enhancement in ductility by delaying the mechanisms at the inception of damage.

6.3. Effect of the grain size ratio

The results presented in the section dedicated to the experimental tensile behavior of all specimens series (see section 4.2 and Figure 7) suggest that both the volume fractions of the grain populations and their respective mean grain sizes influence the mechanical response. The obtained results confirm the trends presented in literature (Berbenni et al., 2007; Flipon et al., 2018a) according to which the effect of the grain size distribution is maximal if an ultra-fine grain matrix is employed. There is indeed no observed effect of the grain size distribution for series 3, which corresponds to samples with a matrix of fine grains (3 μm), whereas there is a significant effect for series 1 and 2, both corresponding to a matrix of ultra-fine grains (0.5 μm). To better illustrate this

phenomenon, the tensile curves of these two specimens series are summarized in Figure 24.

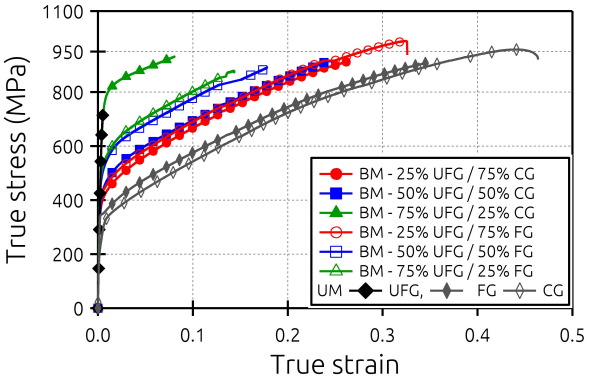

Figure 24: Effect of the grain size ratio on the experimental tensile behavior of bimodal specimens with a matrix of ultra-fine grains (0.5 µm). Open and plain symbols correspond respectively to series 1 and 2, i.e. to a population of coarse grains with a mean size of 3 µm and 15 µm.

Series 1 and 2 differ only by the mean grain size of their coarse grains populations: approximately 3 µm for series 1 and 15 µm for series 2, which leads to two different grain size ratios: of the order of 10 for series 1 and 30 for series 2. For a given volume fraction of ultrafine grains, the mean grain size of a specimen is therefore smaller for series 1 than for series 2 and as a consequence a higher grain size strenghening is expected for series 1. As observed on Figure 24, this phenomenon is confirmed for the specimens with volume fractions UFG/CG equal to 25/75 and 50/50: a higher flow stress is observed with series 1 than with series 2, in particular for the 50/50 specimens. But for the 75/25 specimens, this observation does not stand: the flow stress of series 1 is 200 MPa smaller than the one of series 2.

Different explanations can be prospected regarding this phenomenon. The first one is related to the difference in powders employed for the FG/CG populations. Indeed, differences in intragranular precipitates or chemical composition could impact the mechanical behavior. However, according to TEM analyses (Fig. 6(d)), no large precipitate density has been detected in the coarse grains of series 2 samples. Hence, the potential differences in the employed powders are not sufficient to explain the 200 MPa gap.

The second potential explanation relies on the crystalline nature of the respective powders: single crystal particles for fine grains and polycrystalline particles for coarse grains. As confirmed from EBSD scans of Figure 6, by using single crystalline particles to constitute the coarse grains in a bimodal sample, the probability of obtaining clusters of coarse grains is very low. As reported from numerical analyses, the effect of the bimodal grain size distribution is magnified for clustered configurations; such clusters contribute to larger localization bands and larger low-stress channels and could thus be suspected to decrease the yield stress while delaying fracture to larger strains. But in the experiments, the inverse observation is made: it is the case where coarse grains are

clustered which displays the largest yield stress and the lowest strain to failure.

The third possibility to explain the 200 MPa gap is related to the effect of grain size ratio on the formation and intensity of the low stress channels, which crystal plasticity modeling predicts to develop upon loading. To evaluate this assumption, complementary simulations have been performed on 5 bimodal polycrystals differentiated by their grain size contrasts: the size of ultra-fine grains is the same (set at 0.5 µm), the pair of volume fractions UFG/CG is the same (80/20), there are 4 isolated coarse grains, always at a same locations in the 5 polycrystals (Fig. 25(a,b)), but the chosen mean grain sizes of the coarse grains vary from a polycrystal to the other, leading to 5 grain size ratios: R = 5, 10, 15, 20 and 25.

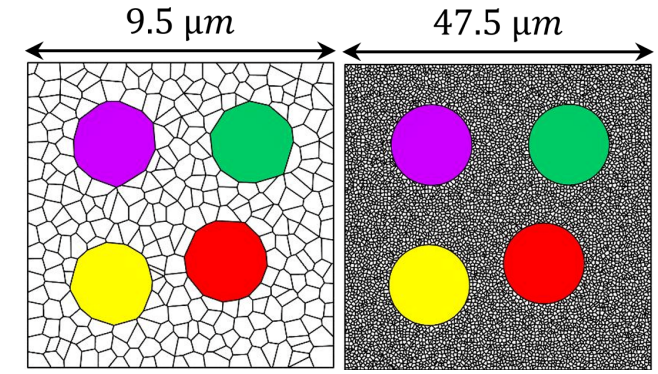

(a) R=5 (b) R=25

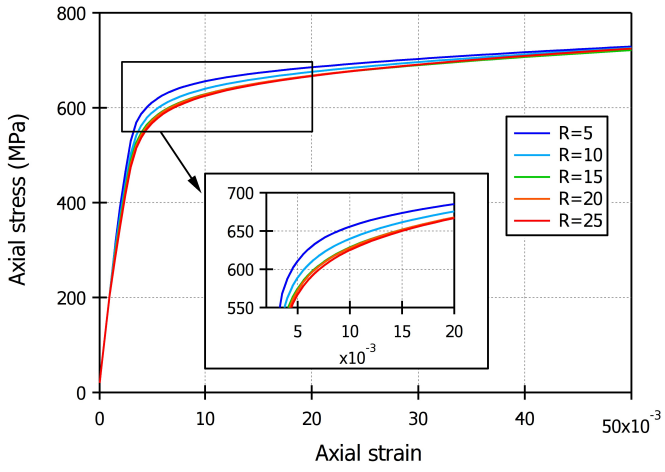

(c)

Figure 25: Effect of the grain size ratio R between the two grain size populations of a bimodal polycrystal with 4 CG. Only the grain size of CG varies from a polycrystal to the other. In (a) and (b), illustrations of the microstructures with R=5 and R=25 and in (c) the simulated tensile curves for five ratios. The size of the UFG population is 0.5 µm for all tested cases.

According to the obtained tensile curves plotted on Figure 25(c), the grain size ratio mainly influences the mechanical response at the beginning of plasticity, when the effect of the grain size distribution is maximal. Moreover, in conformity with the conventionally observed grain size strengthening, the larger the ratio R (i.e. the larger the mean grain size), the smaller the axial stress; this phenomenon is to be related to the width of the low-stress channels which increases as a function of the ratio R. But the experimental analyses lead to the opposite effect of the grain size ratio on strengthening.

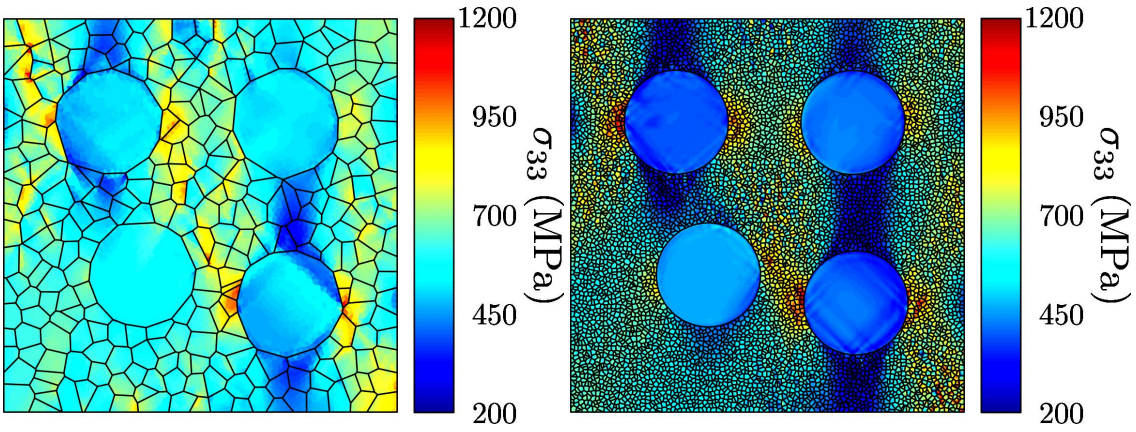

(a) (b)

Figure 26: Axial stress fields for $\varepsilon = 0.005$ imposed strain within the polycrystals of Figure 25: (a) R=5 and (b) R=25. The size of the UFG population is 0.5 µm in both cases.

To summarize, neither the nature of powder particles (in terms of chemical composition, concentrations and sizes of precipitates, and single or multi-crystalline character) nor the difference in grain size ratio can explain why in the particular case of the ultrafine grained matrix with a volume fraction of 75% the highest strength is obtained in the configuration which is not the one expected from modeling. In this particular case, mechanims which are not taken into account in the modeling are thus taking part to the stress-strain behavior. Results from the modeling have revealed heterogeneous plastic strain related to the two grain populations and the formation of shear bands, which comes in agreement with literature (Ma and Zhu, 2017; Ma et al., 2016; Wu et al., 2017, 2015). The possible missing mechanism in the modeling could be related to geometrically necessary dislocations. They are indeed expected to develop as to accomodate the strain gradients which will participate, in turn, to the strain hardening, particularly in the case of ultrafine grains. It is believed that the multiplication of such dislocations could be influenced by the grain size ratio and could then explain the experimental results. Furthermore, these dislocations could also modify the low stress channel intensity close to the coarse grains. A modeling based on strain gradient plasticity could help to confirm this hypothesis and better describe the stress/strain fields of such random bimodal materials.

7. Conclusions

In this article, multiscale experimental and numerical analyses have been performed to examine the influence of grain size distribution on the tensile behavior of a 316L steel. To this purpose, bimodal samples with heterogeneous microstructures have been manufactured from powder metallurgy. In the process of blending coarse grains (CG) and ultrafine grains (UFG), various mean grain sizes, volume fractions and grain size ratios of each grain population have been handled. From the obtained samples, including the reference unimodal alloy made of either UFG or CG, the tensile behaviors have then been characterized: *(i)* from the mean stress-strain responses under monotonic tension and *(ii)* from the decomposition of the flow stress into backstress and thermal or athermal effective stress components using loading-unloading tests. Numerical analyses based on crystal plasticity finite element modeling have been conducted, also for various settings of blends between CG and UFG, and in particular in the distinct situations of either isolated or clustered CG within the matrix of UFG. The main conclusions can be listed as follows:

- Only for fine enough grains (so called *ultrafine* grains, with a size ≤ 1 μm) could one observe an impact of the bimodality. The two main characteristics of the bimodal microstructure affecting the behavior are then the volume fractions in the blend UFG/CG and their respective mean grain sizes.
- Introducing CG within a matrix of UFG leads to two main effects: an increase in ductility of the obtained bimodal polycrystal with respect to the original UFG unimodal polycrystal and a reduction of the flow stress.
- The effect of the bimodal distribution is maximal at the onset of plasticity, which also corresponds to the stage of straining when the contrast in the behaviors of CG and UFG is maximal. This effect is magnified by the presence of clustered coarse grains. It is also tempered as the imposed strain increases: plasticity then expands over larger regions and the contrast in stress responses decreases.
- The aforementioned phenomena of a gain in ductility and a reduction in strength due to the bimodality are well explained by three identified specifics of the micromechanics taking place in the bimodal polycrystal: a reduction in the intergranular backstress and the formation of low stress channels in the UFG matrix which delays the activation of the plasticity within the UFG.

Geometrically necessary dislocations (GND), as opposed to statistically stored dislocations, are known to contribute to a large extent to the plastic strain mechanisms within ultrafine grains and specifically in the presence of high spatially contrasted properties. A more comprehensive understanding of the interactions taking place between the grain size populations could then be accessed by taking these GND into account in the crystal plasticity model.

Acknowledgments

The Normandy region is greatly acknowledged for the financial support of Mathieu Calvat PhD.

References

Arsenlis, A., Parks, D.M., 2002. Modeling the evolution of crystallographic dislocation density in crystal plasticity. Journal of the Mechanics and Physics of Solids 50, 1979 – 2009.

Bach, J., Stoiber, M., Schindler, L., Hppel, H., Gken, M., 2020. Deformation mechanisms and strain rate sensitivity of bimodal andultrafine-grained copper. Acta Materialia 186, 363–373.

Barbe, F., Benedetti, I., Gulizzi, V., Calvat, M., Keller, C., 2020. Elucidating the effect of bimodal grain size distribution on plasticity and fracture behavior of polycrystalline materials. Journal of Multiscale Modelling 11, 2050007.

Barbe, F., Decker, L., Jeulin, D., Cailletaud, G., 2001a. Intergranular and intragranular behavior of polycrystalline aggregates. Part 1: F.E. model. Int. J. Plasticity 17, 513–536. Doi.org/10.1016/S0749-6419(00)00061-9.

Barbe, F., Forest, S., Cailletaud, G., 2001b. Intergranular and intragranular behavior of polycrystalline aggregates. Part 2: results. Int. J. Plasticity 17, 537–563.

Barbe, F., Quey, R., 2011. A numerical modelling of 3D polycrystal-to-polycrystal diffusive phase transformations involving crystal plasticity. Int. J. Plasticity 27, 823–840.

Barbe, F., Quey, R., Musienko, A., Cailletaud, G., 2009. Three-dimensional characterization of strain localization bands in high resolution elastoplastic polycrystals. Mech Res Comm 36, 762–768.

Barbe, F., Quilici, S., Forest, S., Cailletaud, G., 2003. Numerical study of crystalline plasticity: measurements of the heterogeneities due to grain boundaries under small strains. Metallurgical Research & Technology 100, 815–823. Doi.org/10.1051/metal:2003207.

Benedetti, I., Barbe, F., 2013. Modelling Polycrystalline Materials: An Overview of Three-Dimensional Grain-Scale Mechanical Models. Journal of Multiscale Modelling 5, 1–51.

Berbenni, S., Favier, V., Berveiller, M., 2007. Impact of the grain size distribution on the yield stress of heterogeneous materials. International Journal of Plasticity 23, 114 – 142.

Bitzek, E., Brandl, C., Weygand, D., Derlet, P., Van Swygenhoven, H., 2009. Atomistic simulation of a dislocation shear loop interacting with grain boundaries in nanocrystalline aluminium. Modelling and Simulation in Materials Science and Engineering 17, 055008.

Bouchedjra, M., Amrouche, A., Kanit, T., Belouchrani, M., 2020. Microstructural features effect on the evolution of cyclic damage for polycrystalline metals using a multiscale approach. Int. J. Damage Mech. 30, 77–102.

Calvat, M., Flipon, B., Keller, C., Barbe, F., 2021. Accounting for size dependence on the meso- or on the micro-scale in polycrystalline plasticity. A comparative study for different grain size distributions. Springer Nature. chapter 28. Computational and Experimental Simulations in Engineering.

Chaboche, J., 1989. Constitutive equations for cyclic plasticity and cyclic viscoplasticity. Int. J. Plasticity 5, 247–302.

Chang, H., Cordero, N., Déprés, C., Fivel, M., Forest, S., 2016. Micromorphic crystal plasticity versus discrete dislocation dynamics analysis of multilayer pile-up hardening in a narrow channel. Arch. Appl. Mech. 86, 21–38.

Cheng, S., Zhao, Y., Zhu, Y., Ma, E., 2007. Optimizing the strength and ductility of fine structured 2024 al alloy by nano-precipitation. Acta Mater. 55, 5822–5832.

Cordero, N., Gaubert, A., Forest, S., Busso, E., Gallerneau, F., Kruch, S., 2010. Size effects in generalised continuum crystal plasticity for two-phase laminates. J. Mech. Phys. Sol. 58, 1963–1994.

Dao, M., Lu, L., Asaro, R., De Hosson, J.T.M., Ma, E., 2007. Toward a quantitative understanding of mechanical behavior of nanocrystalline metals. Acta Materialia 55, 4041–4065.

Diard, O., Leclercq, S., Rousselier, G., Cailletaud, G., 2005. Evaluation of finite element based analysis of 3D multicrystalline aggregates plasticity. Application to crystal plasticity model identification and the study of stress and strain fields near grain boundaries. Int. J. Plasticity 21, 691–722.

Dickson, J., Boutin, J., Handfield, L., 1984. A comparaison of two simple methods for measuring cyclic internal, effective stresses. Material Science, Engineering 64, L7 – L11.

Dirras, G., Gubicza, J., Ramtani, S., Bui, Q., Szilágyi, T., 2010. Microstructure and mechanical characteristics of bulk polycrystalline ni consolidated from blends of powders with different particle size. Mater. Sci. Engng A 527, 1206–1214.

Doumalin, P., Bornert, M., Crépin, J., 2003. Characterisation of the strain distribution in heterogeneous materials. Mécanique & Industries 4, 607–617.

Duchaussoy, A., Sauvage, X., Deschamps, A., De Geuser, F., Renou, G., Horita, Z., 2021. Complex interactions between precipitation, grain growth and recrystallization in a severely deformed al-zn-mg-cu alloy and consequences on the mechanical behavior. Materialia 15, 101028.

Duchaussoy, A., Sauvage, X., Edalati, K., Horita, Z., Renou, G., Deschamps, A., De Geuser, F., 2019. Structure and mechanical behavior of ultrafine-grained aluminum-iron alloy stabilized by nanoscaled intermetallic particles. Acta Materialia 167, 89–102.

Dunstan, D., Bushby, A., 2014. Grain size dependence of the strength of metals: The hall-petch effect does not scale as the inverse square root of grain size. International Journal of Plasticity 53, 56 – 65.

Etienne, A., Radiguet, B., Cunningham, N., Odette, G., Valiev, R., Pareige, P., 2011. Comparison of radiation-induced segregation in ultrafine-grained and conventional 316 austenitic stainless steels. Ultramicroscopy 111, 659 – 663. Special Issue: 52nd International Field Emission Symposium.

Evers, L.P., Brekelmans, W.A.M., Geers, M.G.D., 2004a. Non-local crystal plasticity model with intrinsic ssd and gnd effects. Journal of the Mechanics and Physics of Solids 52, 2379 – 2001.

Evers, L.P., Brekelmans, W.A.M., Geers, M.G.D., 2004b. Scale dependent crystal plasticity framework with dislocation density and grain boundary effects. International journal of solids and structures 41, 5209 – 5230.

Farooq, H., Cailletaud, G., Forest, S., Ryckelynck, D., 2020. Crystal plasticity modeling of the cyclic behavior of polycrystalline aggregates under non-symmetric uniaxial loading: Global and local analyses. Int. J. Plasticity 126, 102619.

Feaugas, X., Haddou, H., 2003. Grain-size effects on tensile behaviour of nickel, AISI 316L stainless steel. Metallurgical Transactions 34A, 2329 – 2340.

Feaugas, X., Haddou, H., 2007. Effects of grain size on dislocation organization, internal stresses developed under tensile loading in fcc metals. Philosophical Magazine 87, 989 – 1018.

Fleck, N., Muller, G., Ashby, M., Hutchinson, J., 1994. Strain gradient plasticity: Theory and experiment. Acta Metallurgica et Materialia 42, 475 – 487. doi:DOI: 10.1016/0956-7151(94)90502-9.

Flipon, B., 2018. Alliages á grains ultrafins et bimodaux: approche couplée expérience-modélisation basée sur la microstructure. Ph.D. thesis. Normandie Université.

Flipon, B., Garcia de la Cruz, L., Hug, E., Keller, C., Barbe, F., 2017. Elaboration of austenitic stainless steel with bimodal grain size distribution and investigation of their mechanical behavior, 20th Int. ESAFORM Conf. on Material Forming, 26-28 April 2017, Dublin, Ireland, AIP Conference Proceedings 1896, 200007.

Flipon, B., Keller, C., Garci de la Cruz, L., Hug, E., Barbe, F., 2018a. Tensile properties of spark plasma sintered AISI 316L stainless steel with unimodal and bimodal grain size distributions. Materials Science and Engineering: A 729, 249–256.

Flipon, B., Keller, C., Quey, R., Barbe, F., 2020. A full-field crystal-plasticity analysis of bimodal polycrystals. Int. J. Solids Struct. 184, 178–192.

Flipon, B., Milhem, L., Keller, C., Quey, R., Barbe, F., 2018b. Modelling of polycrystals using well-controlled Voronoi-type tessellations and its applications to micromechanical analyses. Presse des Mines. chapter 23. Physics and Mechanics of Random Media: from Morphology to Material Properties, pp. 187–198.

Forest, S., 2008. Some links between cosserat, strain gradient crystal plasticity and the statistical theory of dislocations. Philosophical Magazine 88, 3549–3563.

Forest, S., Barbe, F., Cailletaud, G., 2000. Cosserat modelling of size effects in the mechanical behaviour of polycrystals and multi-phase materials. Int. J. Solids Struct. 37, 7105–7126.

Gérard, C., Cailletaud, G., Bacroix, B., 2013. Modeling of latent hardening produced by complex loading paths in fcc alloys. Int. J. Plasticity 42, 194–212.

Gleiter, H., 1989. Nanocrystalline materials. Prog. Mater. Sci. 33, 223–315.

Guerchais, R., Saintier, N., Morel, F., Robert, C., 2014. Micromechanical investigation of the influence of defects in high cycle fatigue. Int J Fatigue 67, 159–172.

Guery, A., Hild, F., Latourte, F., Roux, S., 2016. Identification of crystal plasticity parameters using dicmeasurements and weightedfemu. Mechanics of Materials 100, 55–71. doi:https://doi.org/10.1016/j.mechmat.2016.06.007.

Guilhem, J., Basseville, S., Curtit, F., Stephan, J., Cailletaud, G., 2018. Numerical analysis of the effect of surface roughness on mechanical fields in polycrystalline aggregates. Mod. Simu. Mater. Sci. Engng 26, 045004.

Hall, E., 1951. The deformation and ageing of mild steel: III discussion of results. Physical Society of London 64, 747 – 753.

Höppel, H., Korn, M., Lapovok, R., Mughrabi, H., 2010. Bimodal grain size distributions in ufg materials produced by spd: Their evolution and effect on mechanical properties, in: Journal of Physics: Conference Series, IOP Publishing. p. 012147.

Hug, E., Prasath Babu, R., Monnet, I., Etienne, A., Moisy, F., Pralong, V., Enikeev, N., Abramova, M., Sauvage, X., Radiguet, B., 2017. Impact of the nanostructuration on the corrosion resistance and hardness of irradiated 316 austenitic stainless steels. Applied Surface Science 392, 1026–1035.

Isaev, N., Grigorova, T., Mendiuk, O., Davydenko, O., Polishchuk, S., Geidarov, V., 2016. Plastic deformation mechanisms of ultrafine-grained copper in the temperature range of 4.2–300 k. Low Temperature Physics 42, 825–835.

Joshi, S., Ramesh, K., Han, B., Lavernia, E., 2006. Modeling the constitutive response of bimodal metals. Metall. Mater. Trans. A 37, 2397–2404.

Keller, C., Hug, E., Feaugas, X., 2011. Microstructural size effects on mechanical properties of high purity nickel. International Journal of Plasticity 27, 635 – 654.

Keller, C., Hug, E., Habraken, A., Duchêne, L., 2012. Finite element analysis of the free surface effects on the mechanical behavior of thin nickel polycrystals. International Journal of Plasticity 29, 155 – 172.

Keller, C., Tabalaiev, K., Marnier, G., Noudem, J., Sauvage, X., Hug, E., 2016. Influence of spark plasma sintering conditions on the sintering and functional properties of an ultra-fine grained 316L stainless steel obtained from ball-milled powder. Materials Science and Engineering: A 665, 125 – 134.

Kurzydłowski, K., Bucki, J., 1993. Flow stress dependence on the distribution of grain size in polycrystals. Acta Metall. Mater. 41, 3141–3146.

Lavergne, F., Brenner, R., Sab, K., 2013. Effects of grain size distribution and stress heterogeneity on yield stress of polycrystals: A numerical approach. Comput. Mater. Sci. 77, 387–398.

Li, J., Cao, Y., Gao, B., Li, Y., Zhu, Y., 2018. Superior strength and ductility of 316l stainless steel with heterogeneous lamella structure. Journal of Materials Science 53, 10442–10456.

Li, J., Zhang, Q., Huang, R., Li, X., Gao, H., 2020. Towards understanding the structure–property relationships of heterogeneous-structured materials. Scripta Materialia 186, 304–311.

Li, Y., Raabe, D., Herbig, M., Choi, P.P., Goto, S., Kostka, A., Yarita, H., Borchers, C., Kirchheim, R., 2014. Segregation stabilizes nanocrystalline bulk steel with near theoretical strength. Physical review letters 113, 106104.

Lin, F., Shi, Q., Delannay, L., 2020. Microscopic heterogeneity of plastic strain and lattice rotation in partially recrystallized copper polycrystals. International Journal of Solids and Structures 184, 167–177. doi:https://doi.org/10.1016/j.ijsolstr.2019.01.024. physics and Mechanics of Random Structures: From Morphology to Material Properties.

Lin, S., Yang, C., Mura, T., Iwakuma, T., 1992. Average elastic-plastic behavior of composite materials. International Journal of Solids and Structures 29, 1859–1872.

Ling, C., Forest, S., Besson, J., Tanguy, B., Latourte, F., 2018. A reduced micromorphic single crystal plasticity model at finite deformations. application to strain localization and void growth in ductile metals. International Journal of Solids and Structures 134, 43–69.

Lu, L., 2004. Ultrahigh strength and high electrical conductivity in copper. Science 304, 422–426.

Lu, X., Zhang, X., Shi, M., Roters, F., Kang, G., Raabe, D., 2019. Dislocation mechanism based size-dependent crystal plasticity modeling and simulation of gradient nano-grained copper. International Journal of Plasticity 113, 52–73. doi:https://doi.org/10.1016/j.ijplas.2018.09.007.

Ludy, J.E., Rupert, T.J., 2016. Amorphous intergranular films act as ultra-efficient point defect sinks during collision cascades. Scripta Materialia 110, 37–40.

Ma, E., 2006. Eight routes to improve the tensile ductility of bulk nanostructured metals and alloys. JOM 58, 49–53.

Ma, E., Zhu, T., 2017. Towards strengthductility synergy through the design of heterogeneous nanostructures in

metals. Materials Today 20, 323–331.
Ma, X., Huang, C., Moering, J., Ruppert, M., Hoppel, H.W., Goken, M., Narayan, J., Zhu, Y., 2016. Mechanical properties of copper/bronze laminates: Role of interfaces. Acta Materialia 116, 43 – 52.
Magee, A., Ladani, L., 2015. Representation of a microstructure with bimodal grain size distribution through crystal plasticity and cohesive interface modeling. Mech. Materials 82, 1–12.
Magee, A., Ladani, L., Topping, T.D., Lavernia, E.J., 2012. Effects of tensile test parameters on the mechanical properties of a bimodal al–mg alloy. Acta materialia 60, 5838–5849.
Marano, A., Gélébart, L., Forest, S., 2021. FFT-based simulations of slip and kink bands formation in 3D polycrystals: Influence of strain gradient crystal plasticity. J. Mech. Phys. Sol. 1497, 104295.
Marnier, G., Keller, C., Noudem, J., Hug, E., 2014. Functional properties of a spark plasma sintered ultrafine-grained 316L steel. Materials & Design 63, 633 – 640.
Méric, L., Cailletaud, G., 1991. Single crystal modeling for structural calculations: Part 2 - finite element implementation. J. Engng Mater. Technol. 113, 171–182.
Méric, L., Poubanne, P., Cailletaud, G., 1991. Single crystal modeling for structural calculations: Part 1- model presentation. J. Engng Mater. Technol. 113, 162–170.
Meyers, M., Mishra, A., Benson, D., 2006. Mechanical properties of nanocrystalline materials. Progress in Materials Science 51, 427 – 556.
Mompiou, F., Tingaud, D., Chang, Y., Gault, B., Dirras, G., 2018. Conventional vs harmonic-structured β-ti-25nb-25zr alloys: A comparative study of deformation mechanisms. Acta Materialia 161, 420–430.
Neper, 2021. Polycrystal generation and meshing. Http://neper.sourceforge.net.
N'Guyen, C., Barbe, F., Osipov, N., Cailletaud, G., Marini, B., Petry, C., 2012. Micromechanical local approach to brittle failure in bainite high resolution polycrystals: A short presentation. Comput. Mater. Sci. 64, 62–65. Doi.org/10.1016/j.commatsci.2012.03.034.
Orlov, D., Fujiwara, H., Ameyama, K., 2013. Obtaining copper with harmonic structure for the optimal balance of structure-performance relationship. Materials transactions 54, 1549–1553.
Pan, Z., Rupert, T.J., 2014. Damage nucleation from repeated dislocation absorption at a grain boundary. Computational materials science 93, 206–209.
Park, H., Ameyama, K., J.Y., Hwang, H., Kim, H., 2018. Additional hardening in harmonic structured materials by strain partitioning and back stress. Materials Research Letters 6, 261–267.
Petch, N., 1953. The cleavage strength of polycrystals. Journal of the Iron Steel Institute 174, 25 – 28.
Phan, V., Nguyen, T., Bui, Q., Dirras, G., 2015. Modelling of microstructural effects on the mechanical behavior of ultrafine-grained nickel using crystal plasticity finite element model. Int. J. Engng Sci. 94, 212–225.
Pineau, A., Benzerga, A., Pardoen, T., 2016. Failure of metals III: Fracture and fatigue of nanostructured metallic materials. Acta Materialia 107, 508 – 544.
Proudhon, H., Li, J., Reischig, P., Guninchault, N., Forest, S., Ludwig, W., 2016. Coupling diffraction contrast tomography with the finite element method. Adv Engng Mater 18, 903–912.
Quey, R., Dawson, P., Barbe, F., 2011. Large-scale 3D random polycrystals for the finite element method: generation, meshing and remeshing. Comput. Meth. Appl. Mech. Engng 200, 1729–1745.
Quey, R., Renversade, L., 2018. Optimal polyhedral description of 3D polycrystals: method and application to statistical and synchotron X-ray diffraction data. Comput. Meth. Appl. Mech. Engng 330, 308–333.
Radiguet, B., Etienne, A., Pareige, P., Sauvage, X., Valiev, R., 2008. Irradiation behavior of nanostructured 316 austenitic stainless steel. Journal of Material Science 43, 7338–7343.
Renk, O., Maier-Kiener, V., Issa, I., Li, J., Kiener, D., Pippan, R., 2019. Anneal hardening and elevated temperature strain rate sensitivity of nanostructured metals: their relation to intergranular dislocation accommodation. Acta Materialia 165, 409–419.
Rupert, T.J., 2016. The role of complexions in metallic nano-grain stability and deformation. Current Opinion in Solid State and Materials Science 20, 257–267. Grain boundary complexions -current status and future directions.
Sathiyamoorthi, P., Kim, H.S., 2020. High-entropy alloys with heterogeneous microstructure: Processing and mechanical properties. Progress in Materials Science , 100709.
Sawicki, A., 1983. Engineering mechanics of elasto-plastic composites. Mechanics of Materials 2, 217–231.
Sergueeva, A., Mara, N., Krasilnikov, N., Valiev, R., Mukherjee, A., 2006. Cooperative grain boundary sliding in

nanocrystalline materials. Philosophical Magazine 86, 5797–5804.
Sharma, B., Miyakoshi, M., Vajpai, S.K., Dirras, G., Ameyama, K., 2020. Extra-strengthening in a harmonic structure designed pure titanium due to preferential recrystallization phenomenon through thermomechanical treatment. Materials Science and Engineering: A 797, 140227.
Shu, J.Y., Fleck, N.A., 1999. Strain gradient crystal plasticity: size-dependent deformation of bicrystals. Journal of the Mechanics and Physics of Solids 47, 297 – 324. doi:DOI: 10.1016/S0022-5096(98)00081-7.
St-Pierre, L., Héripré, E., Dexet, M., Crépin, J., Bertolino, G., Bilger, N., 2008. 3D simulations of microstructure and comparison with experimental microstructure coming from O.I.M. analysis. Int. J. Plasticity 24, 1516–1532.
Taupin, V., Berbenni, S., Fressengeas, C., Bouaziz, O., 2010. On particle size effects: An internal length mean field approach using field dislocation mechanics. Acta Materialia 58, 5532 – 5544. doi:https://doi.org/10.1016/j.actamat.2010.06.034.
Taupin, V., Pesci, R., Berbenni, S., Berveiller, S., Ouahab, R., Bouaziz, O., 2013. Lattice strain measurements using synchrotron diffraction to calibrate a micromechanical modeling in a ferritecementite steel. Materials Science and Engineering: A 561, 67 – 77. doi:https://doi.org/10.1016/j.msea.2012.10.086.
Tingaud, D., Jenei, P., Krawczynska, A., Mompiou, F., Gubicza, J., Dirras, G., 2015. Investigation of deformation micro-mechanisms in nickel consolidated from a bimodal powder by spark plasma sintering. Materials Characterization 99, 118–127.
Vajpai, S., Ota, M., Zhang, Z., Ameyama, K., 2016a. Three-dimensionally gradient harmonic structure design: an integrated approach for high performance structural materials. Mater. Res. Lett. 4, 191–197.
Vajpai, S., Sawangrat, C., Yamaguchi, O., Ciuca, O., Ameyama, K., 2016b. Effect of bimodal harmonic structure design on the deformation behaviour and mechanical properties of Co-Cr-Mo alloy. Mater. Sci. Engng C 58, 1008–1015.
Vajpai, S.K., Ota, M., Watanabe, T., Maeda, R., Sekiguchi, T., Kusaka, T., Ameyama, K., 2015. The development of high performance ti-6al-4v alloy via a unique microstructural design with bimodal grain size distribution. Metallurgical and Materials Transactions A 46, 903–914.
Van Swygenhoven, H., Derlet, P., 2001. Grain-boundary sliding in nanocrystalline fcc metals. Physical review B 64, 224105.
Van Swygenhoven, H., Derlet, P., Frøseth, A., 2006. Nucleation and propagation of dislocations in nanocrystalline fcc metals. Acta Materialia 54, 1975–1983.
Wang, X., Cazes, F., Li, J., Hocini, A., Ameyama, K., Dirras, G., 2019. A 3d crystal plasticity model of monotonic and cyclic simple shear deformation for commercial-purity polycrystalline ti with a harmonic structure. Mechanics of Materials 128, 117 – 128. doi:https://doi.org/10.1016/j.mechmat.2018.10.006.
Wang, Y., Huang, C., Fang, X., Hppel, H., Gken, M., Zhu, Y., 2020. Hetero-deformation induced (hdi) hardening does not increase linearly with strain gradient. Scripta Materialia 174, 19–23.
Wang, Y., Voisin, T., McKeown, J., Ye, J., Calta, N., Li, Z., Zeng, Z., Zhang, Y., Chen, W., Roehling, T., 2018. Additively manufactured hierarchical stainless steels with high strength and ductility. Nature materials 17, 63.
Wu, H., Niu, G., Cao, J., Yang, M., 2017. Annealing of strain-induced martensite to obtain micro/nanometre grains in austenitic stainless. Materials Science and Technology 33, 480–486.
Wu, X., Yang, M., Yuan, F., Wu, G., Wei, Y., Huang, X., Zhu, Y., 2015. Heterogeneous lamella structure unites ultrafine-grain strength with coarse-grain ductility. Proceedings of the National Academy of Sciences 112, 14501–14505.
Wu, X., Zhu, Y., 2017. Heterogeneous materials: a new class of materials with unprecedented mechanical properties. Materials Research Letters 5, 527–532.
Yang, S., Dirrenberger, J., Monteiro, E., Ranc, N., 2019. Representative volume element size determination for viscoplastic properties in polycrystalline materials. International Journal of Solids and Structures 158, 210–219. doi:https://doi.org/10.1016/j.ijsolstr.2018.09.011.
Z-set, 2021. Non-linear material & structure analysis suite). Http://www.zset-software.com.
Zhang, Z., Ma, H., Zheng, R., Hu, Q., Nakatani, M., Ota, M., Chen, G., Chen, X., Ma, C., Ameyama, K., 2017. Fatigue behavior of a harmonic structure designed austenitic stainless steel under uniaxial stress loading. Materials Science and Engineering: A 707, 287–294.
Zhang, Z., Orlov, D., Vajpai, S., Tong, B., Ameyama, K., 2015a. Importance of bimodal structure topology in the

control of mechanical properties of a stainless steel. Adv. Eng. Mater. 17, 791–795.
Zhang, Z., Orlov, D., Vajpai, S.K., Tong, B., Ameyama, K., 2015b. Importance of bimodal structure topology in the control of mechanical properties of a stainless steel. Advanced Engineering Materials 17, 791–795.
Zhang, Z., Vajpai, S., Orlov, D., Ameyama, K., 2014. Improvement of mechanical properties in SUS304L steel through the control of bimodal microstructure characteristics. Mater. Sci. Engng A 598, 106–113.
Zheng, Z., Liu, J., Gao, Y., 2017. Achieving high strength and high ductility in 304 stainless steel through bi-modal microstructure prepared by post-ecap annealing. Materials Science and Engineering: A 680, 426–432.
Zhu, B., Asaro, R., Krysl, P., Zhang, K., Weertman, J., 2006. Effects of grain size distribution on the mechanical response of nanocrystalline metals: Part II. Acta Mater. 54, 3307–3320.
Zhu, L., Lu, J., 2012. Modelling the plastic deformation of nanostructured metals with bimodal grain size distribution. Int. J. Plasticity 30-31, 166–184.
Zhu, Y., Langdon, T., 2005. Influence of grain size on deformation mechanisms: an extension to nanocrystalline materials. Mater. Sci. Engng A 409, 234–242.
Zhu, Y., Wu, X., 2019. Perspective on hetero-deformation induced (hdi) hardening and back stress. Materials Research Letters 7, 393–398.
Zouaghi, A., Velay, V., Soveja, A., Pottier, T., Cheikh, M., Rézaı-Aria, F., 2016. A multi-scale approach to investigate the nonlinear subsurface behavior and strain localization of X38CrMoV5-1 martensitic tool steel: Experiment and numerical analysis. Int. J. Plasticity 87, 130–153.